Multidisciplinary Design Optimization of Transonic Wings with Boundary Layer Suction

V. Mosca*, A. Sudhi[†]
Technical University of Braunschweig, Cluster of Excellence SE²A – Sustainable and Energy-Efficient Aviation, Braunschweig, Germany

C. Badrya[‡]
The University of California Davis, Davis, CA USA 95616

A. Elham[§]
University of Southampton, Southampton SO16 7QF, United Kingdom

A quasi-three-dimensional aerodynamic solver is developed for aerodynamic analysis of wings in a transonic regime, able to capture the effect of Boundary Layer Suction (BLS) in Hybrid Laminar Flow Control (HLFC) application or transition to turbulent flow for Natural Laminar Flow (NLF). The tool provides accurate results but without the high computational cost of high-fidelity tools. The solver combines the use of an Euler flow solver characterized by an integral boundary layer method and Linear Stability Analysis using a 2.75D approximation for transition prediction. In particular, a conical transformation is adopted, including the determination of the shock-wave position. The solver is implemented in a Multidisciplinary Design Optimization (MDO) framework, including wing weights estimation and aircraft performance analysis. The framework consists of different modules: aerodynamics, structure, suction system analysis, and performance evaluation. Using a genetic algorithm and considering HLFC technology, wing MDO has been performed to find the optimum wing planform and airfoil shape. A backward swept wing aircraft, developed inside the Cluster of Excellence SE²A (Sustainable and Energy Efficient Aviation) is studied. Novel technologies such as active flow control, limited maximum load factor due to load alleviation and novel materials allow a fuel weight reduction of 6%.

Nomenclature

α	=	angle-of-attack, deg
Γ	=	dihedral angle, deg
η	=	efficiency

*Phd candidate, Institute of Aircraft Design and Lightweight Structures, v.mosca@tu-braunschweig.de.
†Phd candidate, Institute of Fluid Mechanics, a.sudhi@tu-braunschweig.de
‡Assistant Professor, Department of Mechanical and Aerospace Engineering, cbadrya@ucdavis.edu.
§Professor, Department of Aeronautics and Astronautics, Computational Engineering and Design Group, a.elham@soton.ac.uk.

λ	=	taper-ratio
φ	=	sweep angle
AR	=	aspect ratio
BLS	=	boundary layer suction
b	=	span, m
C_d	=	sectional drag coefficient
C_D	=	wing drag coefficient
C_{ds}	=	sectional suction drag coefficient
C_{Ds}	=	wing suction drag coefficient
C_l	=	sectional lift coefficient
C_L	=	wing lift coefficient
c	=	chord, m
c_m	=	pitching moment
E^*	=	energy density, Wh/kg
HLFC	=	hybrid laminar flow control
J	=	fitness function
L/D	=	lift-to-drag ratio
LFC	=	laminar flow control
M	=	Mach number
MTOW	=	maximum take-off weight, kg
OEW	=	operating empty weight, kg
P	=	power, W
R	=	range, km
Re	=	Reynolds number
S	=	Surface, m^2
t	=	thickness
T/W	=	thrust-to-weight ratio
V	=	cruise speed
W	=	weight, kg
W/S	=	wing loading kg/m^2

Subscripts

| b | = | battery |

f	=	fuel
i	=	induced
r	=	root
t	=	tip
TO	=	take-off
w	=	wing

I. Introduction

Climate changes and economic crises push European governments to develop a common strategy to cut emissions and design the new generation of aircraft. Flightpath 2050 [1] establishes optimistic objectives for the future of aviation, like reducing 75% and 90% of CO_2 and NO_x emission, respectively, and a 65% noise reduction. Current technologies could be used at higher efficiencies to achieve these goals, but the possible growth trend of air transportation may need substantial developments, like active flow control, load alleviation, boundary layer ingestion, and advanced structures.

Boundary layer suction (BLS) represents a well-known technique for drag reduction. In fact, wind-tunnel experimental work on Laminar Flow Control (LFC) for aviation was performed in the late 1930s [2]. Natural Laminar Flow (NLF) airfoils are able to passively reach laminar flow through a proper airfoil shape design. This phenomenon is reached in the forward part of the airfoil and with a limited leading edge sweep angle. The increment of sweep (>18 deg) leads to relevant Cross Flow Instabilities (CFI) and Attachment Line Transition (ALT), in addition to Tollmien–Schlichting Instabilities (TSI) [3, 4]. The dominance of CFI and ALT near the leading edge limits NLF design to lower Reynolds numbers [5, 6]. Boundary Layer Suction (BLS) removes a small amount of flow, at low momentum, in the wall region. In this way, instabilities are damped, and the boundary layer is stabilized. The effect of a higher sweep angle and higher Reynolds number may be mitigated. Airfoil shape tailoring allows for laminar flow downstream. The couple of BLS with natural laminar flow is called Hybrid Laminar Flow Control (HLFC). Since the mid-1980s, the research was mainly focused on HLFC [7]. Recently, Boeing has mounted a HLFC system for the horizontal and vertical tail of its B787-9, benefits are reported as "significant" [8]. Beck et al. [9] studied a mid-range forward-swept wing configuration with an 80% laminar flow wing and a 70% laminarized fuselage, with a potential fuel burn reduction up to 47%. Sudhi et al. performed a 2D airfoil shape optimization for subsonic unswept [10] and transonic swept wing in NLF and HLFC applications [11] to minimise drag and for power optimization. In the transonic regime, the optimum NLF airfoil has 27% lower drag than an optimum turbulent airfoil, while the optimum HLFC airfoil showed a 25% lower total drag than the NLF airfoil [11]. Design optimization of a fully-electric regional airplane with HLFC is studied in [12], showing a reduction of profile drag of more than 38% achieved using BLS.

Load alleviation via passive or active technologies represents an approach to reduce bending moments and hence

structural weight reduction. A lower maximum bending moment allows designing wings for a lower limit load factor. Passive load alleviation is mainly established by designing the structure in a way that, when subjected to high loads, its deformation reduces the lift. Techniques include nonlinear stiffness material design [13], viscoelastic damping design [14], new structural concepts [15, 16], and finally, local morphing structures [13]. Hahn et al. [17] performed a coupled fluid-structure-interaction analysis; the concept includes a structure which buckles at a critical load higher than cruise lift and consequent deformation that reduces the lift itself. Active load alleviation is applied through wing flow control, implying a more favorable load distribution and hence a reduced wing bending moment. In particular, investigations on the feasibility of the use of active load alleviation technology are done by Rossow et al. [18]; Liu et al. [19] designed robust control laws for a large flexible wing with uncertainty in Mach number and dynamic pressure to investigate the load reduction capability by use of a controller.

In literature, different frameworks are designed for wing aerostructural optimization. Low-fidelity tools are limited for aerostructural optimizations. In fact, the estimation could be subjected to inaccuracies making them more suitable for preliminary and initial design as done in [20]. At the opposite, high-fidelity tools can be applied for aerodynamic and structural refinements, able to capture the effects of aerostructural phenomena not really visible at low fidelity. However, high-fidelity analysis implies high computational power, cost and in general, experience to set the problem correctly. An example can be represented by Liem et al. [21], in which a structural wing analysis is obtained through a finite element analysis tool, while the aerodynamics part is investigated for an inviscid and incompressible flow. These data are then used to build a surrogate model. Therefore, a medium-fidelity approach represents a trade-off between acceptable computational power and accuracy in the analysis. In Mosca et al. [22], a mid-fidelity aerostructural optimization framework is presented, characterized by the coupled adjoint sensitivity analysis method [23] in order to facilitate the gradient computation. The framework is able to capture in a mid-fidelity approach the aeroelastic effect but lacks a mid-fidelity accuracy for boundary layer suction estimation; in fact, the technology is simulated through a drag penalty method and without any modification or study of the boundary layer equations.

This work aims to present a medium fidelity but physics-based analysis including a framework for wing aerostructural optimization for HLFC and NLF application, able to compute structural and aerodynamic parameters considering the novel technologies. In this study, a particular focus is given to active flow control technology utilizing boundary layer suction (BLS). The framework presents different modules studying: aerodynamics, structure and propulsion. The aerodynamic module consists of an Euler-based solver, boundary layer solver and linear stability theory (LST). The structural block uses elementary wing box sizing techniques to compute the amount and distribution of material necessary to sustain the applied loads, combined with empirical methods to estimate the other weight contributions. The propulsion module presents empirical techniques to estimate performance parameters and fuel weight. A Genetic Algorithm (GA) is used due to the high convexity of the design space. In fact, the aerodynamic module may suffer from convergence issues, making the gradient computation difficult. Hence, a gradient-free optimization results in higher

4

robustness. In this way, the optimizer has a lower probability of getting stuck in local optima, having the possibility to explore a wider solution space. A backward-swept mid-range aircraft developed in the Cluster of Excellence SE^{2}A (Sustainable and Energy Efficient Aviation) [24] is studied. The SE^{2}A is an interdisciplinary research center developed in Germany to pursue the above-mentioned objectives for sustainable aviation by investigating different technologies. The present work is divided into several sections. Section II presents laminar flow control technology and its implementation within the framework, while section III describes a new Quasi-Three-Dimensional tool for HLFC (Q3D-HLFC) application providing details about the methodology implemented for wing drag and loads estimation. Section IV presents details about the optimization framework, including design variables, constraints and the modules involved. Section V gives details about the results. In the last section, conclusions are defined.

II. Laminar flow control

The section focuses on the theoretical explanations of the fundamentals of laminar flow control. The technique is used to extend the laminar flow over the wing by dampening the amplified instabilities, which cause the transition to turbulent flow. On a wing, three different instabilities can be studied: 1) Tollmien–Schlichting Instabilities (TSI), 2) Cross-Flow Instabilities (CFI), and 3) Attachment-Line Instabilities (ALI). TSI are given by disturbance waves that travel in a streamwise direction, generally occurring behind the maximum airfoil thickness due to the amplification provided by positive pressure gradient [25]. CFI originate from the streamline curvature characteristic in three-dimensional boundary layers. Higher sweep angles increase them due to additional pressure gradient along the wingspan and the associated three-dimensionality of the boundary layer. In particular, they act close to the leading edge where there is a strong adverse pressure gradient [25]. ALI represent another disturbance related to three-dimensional flow. In particular, when significant disturbances occur for swept wings, an example is given by the turbulent boundary layer of the fuselage, and their propagation along the attachment line may result in transition [26]. Boundary layer and linear stability theory (LST) solvers, COCO-LILO [27, 28] are used to extract laminar boundary layer characteristics and for laminar to turbulent transition prediction, including the effect of boundary layer suction (BLS). The profile drag, decomposed in pressure and friction drag, is evaluated through MSES [29] for pressure drag and turbulent skin friction drag. In contrast, the laminar skin friction drag is obtained from the boundary layer code. If a boundary layer is assumed thin with respect to the characteristic length ($\delta'=\delta/l \ll 1$) and large Reynolds number (Re$\rightarrow \infty$), terms of the order O(δ') or smaller in the Navier-Stokes equation can be neglected [25]. Considering a two-dimensional, steady, compressible flow which velocity components are u and v in x and y direction, the flow density ρ, static pressure P, the boundary layer equations consist of:

x momentum equation:

$$u\frac{\delta\rho u}{\delta x} + v\frac{\delta\rho u}{\delta y} = -\frac{\delta P}{\delta x} + \mu\frac{\delta^2 u}{\delta^2 y} \tag{1}$$

y momentum equation:

$$0 = -\frac{\delta P}{\delta y} \tag{2}$$

Continuity equation:

$$\frac{\delta \rho u}{\delta x} + \frac{\delta \rho v}{\delta y} = 0 \tag{3}$$

Boundary conditions: y = 0; u = 0; $v = v_0$ (< 0 for suction); $y \to \infty : u \to U(x)$

At the wall (y = 0):

$$v_0 \left(\frac{\delta \rho u}{\delta y} \right)_0 = -\frac{\delta p}{\delta x} + \mu \frac{\delta^2 u}{\delta^2 y} \tag{4}$$

The curvature of the velocity profile $\frac{\delta^2 u}{\delta^2 y}$ in Eq.4 influences the stability of the laminar boundary layer. In particular, the more negative the term is, the more stabilized the flow [25, 30]. Hence, analyzing (Eq.4), it can be passively controlled by pressure gradient and actively by imparting a normal velocity at the wall ($v_0 < 0$ for BLS). The combination of a favorable pressure gradient and BLS, maintaining the boundary layer stability, represents the principle of HLFC. The shock-wave location gives the maximum portion of laminar flow achievable for a typical transonic flow, in fact, the adverse pressure across the shock makes the laminar flow separate. The suction effect across the shock is not studied in this work.

III. Quasi-Three-Dimensional Hybrid Laminar Flow Control Aerodynamic Solver

The Quasi-Three-Dimensional Hybrid Laminar Flow Control (Q3D-HLFC) Aerodynamic Solver represents a substantially modified Quasi-Three-Dimensional (Q3D) methodology [31], able to capture NLF or HLFC effect. The tool is used in the aerodynamic module of the optimization framework for drag computation. The new Q3D can directly compute the shock-wave position in the MSES-COCO-LILO module and the application of a conical transformation of the airfoil section as deeply studied in [30, 32]. Drag is decomposed into different components: friction, pressure (including wave drag) and induced drag. Miscellaneous drag, caused by small components like surface imperfections, is not taken into account in this analysis. For simplification, considering the pressure nature of the wave drag and the dependence on the airfoil shape, they are lumped into one single component defined as pressure drag that, together with friction, defines the profile drag. Another drag source is considered when active flow control is applied: suction drag. In fact, the use of BLS implies an energetic dispense due to the pressure losses given by the suction system that needs to be considered when sizing the aircraft. The Q3D-HLFC consists of three steps: 1) a Vortex Lattice Method (VLM) is used to calculate the lift distribution, loads and lift coefficient C_L. Besides, wing induced drag is obtained using the Trefftz plane analysis [33]; 2) outputs from step 1 are used to run the airfoil analysis tool given by the coupling MSES-COCO-LILO. The tool is applied for each two-dimensional (2D) section where the wing is divided to compute pressure and suction distribution, transition location and profile drag. Conical-flow assumptions are used to take into

account three-dimensional (3D) effects, and so to move from a 2D to an approximated 3D approach [30]. Step 3) is about the computation of the wing total drag and suction power. Some strategies for non-converged cases may be used. The whole Q3D-HLFC framework is shown in Fig.1.
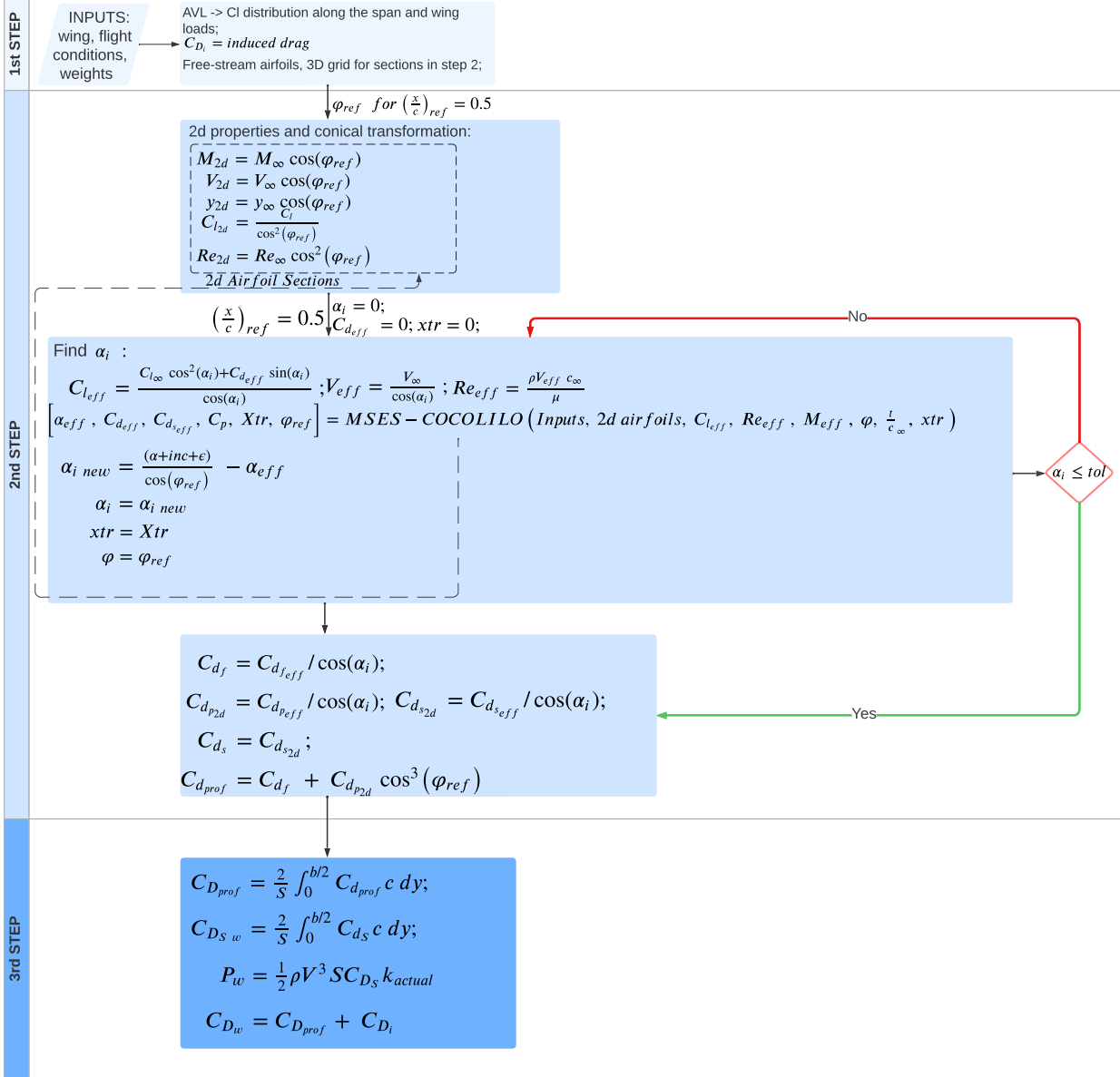

1st STEP

INPUTS: wing, flight conditions, weights

AVL -> Cl distribution along the span and wing loads;
$C_{D_i} = induced\ drag$
Free-stream airfoils, 3D grid for sections in step 2;

2nd STEP

$\varphi_{ref}\ \ for\ \left(\frac{x}{c}\right)_{ref} = 0.5$

2d properties and conical transformation:

$M_{2d} = M_\infty \cos(\varphi_{ref})$
$V_{2d} = V_\infty \cos(\varphi_{ref})$
$y_{2d} = y_\infty \cos(\varphi_{ref})$
$C_{l_{2d}} = \frac{C_l}{\cos^2(\varphi_{ref})}$
$Re_{2d} = Re_\infty \cos^2(\varphi_{ref})$
2d Airfoil Sections

$\left(\frac{x}{c}\right)_{ref} = 0.5 \Big|\begin{array}{l}\alpha_i = 0; \\ C_{d_{eff}} = 0; xtr = 0;\end{array}$

Find α_i :

$C_{l_{eff}} = \frac{C_{l_\infty}\cos^2(\alpha_i)+C_{d_{eff}}\sin(\alpha_i)}{\cos(\alpha_i)}$; $V_{eff} = \frac{V_\infty}{\cos(\alpha_i)}$; $Re_{eff} = \frac{\rho V_{eff}\ c_\infty}{\mu}$

$\left[\alpha_{eff}\ ,\ C_{d_{eff}},\ C_{d_{s_{eff}}},\ C_p,\ Xtr,\ \varphi_{ref}\right] = MSES - COCOLILO\left(Inputs,\ 2d\ airfoils,\ C_{l_{eff}},\ Re_{eff}\ ,\ M_{eff}\ ,\ \varphi,\ \frac{t}{c}_\infty,\ xtr\right)$

$\alpha_{i\ new} = \frac{(\alpha+inc+\epsilon)}{\cos(\varphi_{ref})} - \alpha_{eff}$

$\alpha_i = \alpha_{i\ new}$

$xtr = Xtr$

$\varphi = \varphi_{ref}$

No

$\alpha_i \leq tol$

$C_{d_f} = C_{d_{f_{eff}}}/\cos(\alpha_i);$

$C_{d_{p2d}} = C_{d_{p_{eff}}}/\cos(\alpha_i);\ C_{d_{s2d}} = C_{d_{s_{eff}}}/\cos(\alpha_i);$

$C_{d_s} = C_{d_{s2d}};$

$C_{d_{prof}} = C_{d_f}\ +\ C_{d_{p2d}}\cos^3(\varphi_{ref})$

Yes

3rd STEP

$C_{D_{prof}} = \frac{2}{S}\int_0^{b/2} C_{d_{prof}}c\ dy;$

$C_{D_{S\ w}} = \frac{2}{S}\int_0^{b/2} C_{d_S}c\ dy;$

$P_w = \frac{1}{2}\rho V^3 SC_{D_S}k_{actual}$

$C_{D_w} = C_{D_{prof}}\ +\ C_{D_i}$

Fig. 1   Q3D-HLFC flow chart.

A. Q3D-HLFC Description

1. Step 1

Airfoil shapes, geometrical parameters and wing lift coefficient C_L (or the angle of attack α) represent inputs for the VLM like the Athena Vortex Lattice (AVL) [34] from which the lift distribution along the span and in general

wing loads are obtained. Lift coefficient C_L is determined in case α is used as input, or at the opposite, in case of lift coefficient is provided, then the angle of attack is obtained, induced drag C_{Di} is calculated from Trefftz theory [33].

2. Step 2

The wing is divided into eight sections, generated parallel to the free-stream. In fact, the free-stream properties are computed because they are needed as input of the COCO-LILO module. Each free-stream property is converted according to a 2D conical transformation, considering a reference angle φ_{ref}, as input of MSES. The division into eight spanwise sections represents an effective trade-off between accuracy and computational cost, as proofed in [31]. A higher number of sections improve the accuracy slightly but with a substantial increment of computational time. The reference angle represents the local sweep angle for which $(x/c)_{ref}=(x/c)_{shock-wave}$. Lock equivalence law defines the transformation, from a geometrical and flow point of view, between the free-stream reference frame (represented by the subscript ∞) and the conical reference frame sections (subscript $2d$) [35]. The main parameters, Mach number M, speed V, y-coordinate along the wing span and sectional lift coefficient C_l, expressed for the conical sections, are defined as:

$$M_{2d} = M_\infty cos(\varphi_{ref}) \tag{5}$$

$$V_{2d} = V_\infty cos(\varphi_{ref}) \tag{6}$$

$$y_{2d} = y_\infty cos(\varphi_{ref}) \tag{7}$$

$$C_{l_{2d}} = C_{l_\infty}/cos^2(\varphi_{ref}) \tag{8}$$

The airfoil transformation for a wing swept-tapered segment is done considering an equivalent airfoil developed along a conical arc chord. Its origin lies in a virtual wing apex V, from which all lines at constant chord fraction are generated. The methodology has been studied and applied in Kaups and Cebeci [36], and at the Deutsches Zentrum für Luft- und Raumfahrt (DLR) [30, 32]. In details:

$$tan(\varphi) = tan(\varphi_{le})\left(1 - \frac{x}{c}\right) + tan(\varphi_{te})\left(\frac{x}{c}\right) \tag{9}$$

$$\left(\frac{z}{c}\right)_{conical} = \left(\frac{z}{c}\right)_{3d}\sqrt{1 + [tan(\varphi_{le})\left(1 - \frac{x}{c}\right) + tan\left(\frac{x}{c}\right)]^2} \tag{10}$$

where φ represents the sweep angle, while x/c and z/c are the nondimensionalized airfoil coordinates. The wing transformation is shown in Fig.2. In particular, the wing is divided into different segments depending on the geometrical variations. As an example, the reference wing shown in Fig.2 shows two different segments, limited by the blue sectional line, dividing the wing between the root and the kink, and then from the kink to the tip. The leading and trailing edge

sweep angles change depending on the geometry of the segment considered. Besides, the picture shows an example of isobars drawn assuming isochord lines $((x/c)_{const})$ and the local sweep angle φ between the section and the considered isobar. The dashed line shows the transformed conical arc for the airfoil section. The strategy is reasonable, especially if the distance between the apex and the conical wing element is sufficiently large. This condition is satisfied in the case of moderate taper ratios [27]. The division of the wing into different segments, depending on the geometrical variations, helps the satisfaction of the previous conditions, as visible in Fig.2.
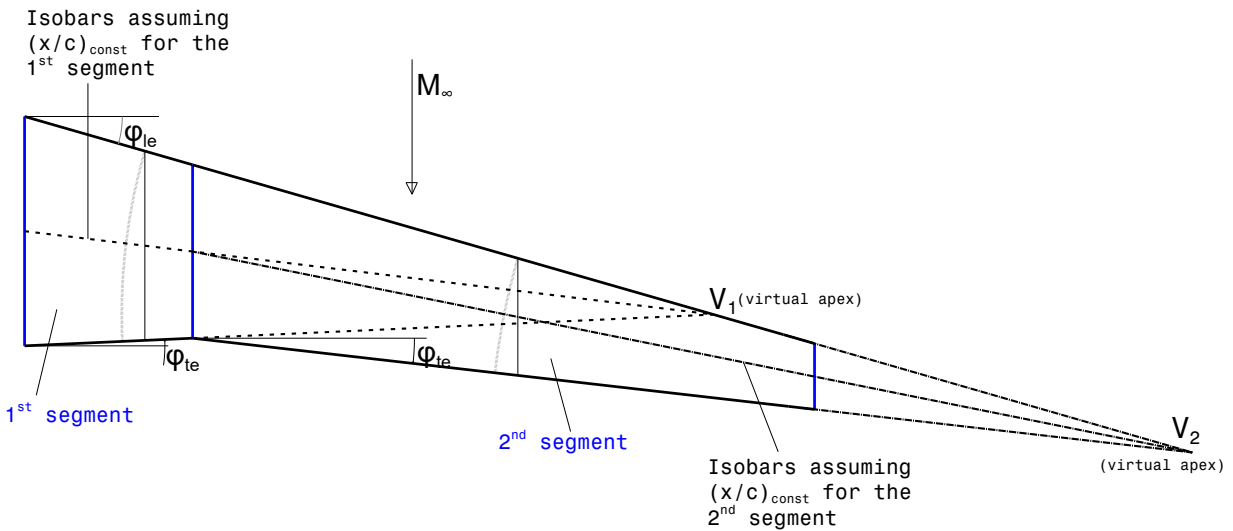
Fig. 2   Wing conical transformation.

The core part of the methodology is the determination of the sectional drag coefficient considering sweep and taper ratio; the calculation relies on an iterative process in which the induced angle of attack α_i is found. The tool allows the possibility of determining the two-dimensional sections according to a conical transformation or perpendicular to the sweep-line drawn 25% chord-wise for subsonic cases, while 50% chord-wise as an approximation for transonic regime application. The first solution, applied in this research, is represented by the airfoil conical transformation and by the reference sweep angle obtained with respect to the calculated shock-wave line. The technique is generally referred to as "2.75D" [32]. According to the last two solutions, the user can fix the local sweep line used to obtain the angles needed to convert sectional properties to free-stream at 25% chord if low subsonic or 50% for transonic regime

and then produce normal sections to this line. The approximation is called "2.5D". A 2.5D approximation generally assumes an infinitely swept wing without considering the effects of wing taper. In fact, properties are transformed into a leading-edge normal 2D reference frame. In this research, because airfoils are generated considering geometrical wing variations, taper-ratio is always considered, even for a 2.5D analysis in which the sweep/shock line used to convert properties is fixed. The main difference between the two approaches lies in generating sections and flow properties with respect to a 2D reference frame considering exactly the sweep angle between the shock position and the horizontal axis in the case of a 2.75 analysis. An intermediate solution that can also be applied in the tool is the use of a conical transformation but fixing the shock-line chord position to estimate the local sweep angle. Considering the forces and angles shown in Fig.3, the effective lift referred to free-stream condition is given by:

$$l_{eff} = \frac{l_\infty + d_{eff} sin(\alpha_i)}{cos(\alpha_i)} \tag{11}$$

where d_{eff} is the effective drag, α_i is the induced angle of attack. In particular:

$$l_{eff} = \frac{1}{2}\rho V_{eff}{}^2 c_\infty C_{l_{eff}} \tag{12}$$

$$l_{2D} = \frac{1}{2}\rho V_\infty{}^2 c_\infty C_{l_\infty} \tag{13}$$

$$d_{eff} = \frac{1}{2}\rho V_{eff}{}^2 c_\infty C_{d_{eff}} \tag{14}$$

$$V_{eff} = \frac{V_\infty}{cos(\alpha_i)} \tag{15}$$

having defined the flow density as ρ and the aerodynamic chord c. Hence, the effective lift coefficient is expressed as:

$$C_{l_{eff}} = \frac{C_{l_\infty} cos(\alpha_i)^2 + C_{d_{eff}} sin(\alpha_i)}{cos(\alpha_i)} \tag{16}$$

While the effective Reynolds number:

$$Re_{eff} = \frac{\rho V_{eff} c_\infty}{\mu} \tag{17}$$

An aerodynamic solver, consisting of the coupling of MSES and COCO-LILO, is used for drag analysis. In particular, it receives effective free-stream conditions and converts these parameters for the 2D conical sections using the equations listed, from Eq.5 to Eq.8, as input of MSES. The initial reference sweep angle is given by φ_{ref} for $(x/c)_{ref} = 0.5$.
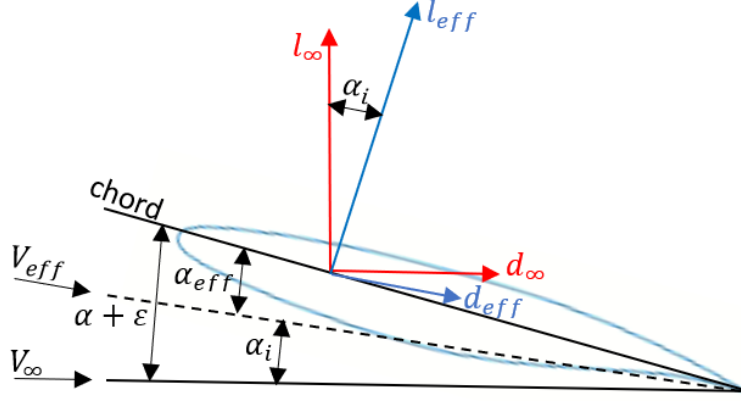
Fig. 3 Wing section angles and forces.

.

Inside this block, the shock-wave location is computed and becomes the new $(x/c)_{ref}$, the value is updated until the transition point x_{tr} is determined and converged. The lift coefficient value used for MSES needs to be transformed for the 2D conical section considering the term of effective drag as seen in Eq.16 and considering a coefficient $K_{C_{d_{eff}}} = C_{d_{eff}} sin(\alpha_i)/cos(\alpha_i)$. Hence:

$$C_{l_{2deff}} = (C_{l_{2deff}} - K_{C_{d_{eff}}})/cos^2(\varphi_{ref}) + K_{C_{d_{eff}}} \tag{18}$$

In this way, the proper C_l is selected for MSES analysis, while the COCO-LILO block will receive the free-stream one initially computed. Besides, the MSES-COCO-LILO toolbox has generic inputs for the AVL and the optimization framework, including suction parameters and efficiencies. The tool also needs $C_{l_{eff}}$, Re_{eff}, M_{eff}, the local sweep angle φ (computed between the horizontal and the sweep line for the local chord), and t/c_∞ representing the thickness to chord ratio for the sections according to the free stream. The parameter is used to take into account attachment-line instabilities (see Sec.III.B) and for the BLS weights computation, treated in the following modules of the MDO (see Sec.IV.C). Besides, the module receives the transition location for the upper and lower surface as input. The new induced angle of attack $\alpha_{i_{new}}$ is given considering the incidence angle (α) given as input (0 deg for our cruise mission) and the geometrical twist angle (ϵ) transformed according to the sectional direction and then subtracting with the effective angle of attack α_{eff} obtained by MSES. In fact:

$$\alpha_i = \frac{\alpha + \epsilon}{cos(\varphi_{ref})} - \alpha_{eff} \tag{19}$$

The new induced angle of attack will be used to obtain the new effective properties iterating until the tolerance is satisfied. The reference sweep angle is updated at each iteration. Therefore, the solver may be launched multiple times. Hence, the last transition location for the upper and lower surface is taken to reduce the number of iterations for the

11

convergence of COCO-LILO. Initially, a full turbulent case is supposed. Therefore a transition position for the upper and lower surface is given by: $x_{tr} = [0\ 0]$.

In our research, instead of using a near-field analysis term to consider induced drag, a far-field approach, given by AVL in step 1 (Sec.III.A.1), is chosen for its higher accuracy. The profile drag coefficient can be decomposed in friction and pressure drag (including wave drag) according to a 2D section analysis, while the suction drag is defined similarly for the same 2D approach:

$$C_{d_f} = \frac{C_{d_{f_{eff}}}}{cos(\alpha_i)} \qquad C_{d_{P2d}} = \frac{C_{d_{P_{eff}}}}{cos(\alpha_i)} \qquad C_{d_{s_{2d}}} = \frac{C_{d_{s_{eff}}}}{cos(\alpha_i)} \tag{20}$$

Sweep theory needs to be applied to compute the profile drag in the free-stream direction (see Fig.2). Drela in [37] assumes that friction drag, considering its nature given by the friction vector τ_w mostly aligned with the outer potential flow and generally parallel to V_∞, is scaled with the free-stream dynamic pressure, while pressure drag due to shock-wave and viscous displacement is assumed to scale with the dynamic pressure according to the normal direction of the wing and acting normal to the sweep/shock-wave line. Suction drag represents the "energetic" cost necessary for BLS, considering the difference in pressure between the free-stream and boundary layer edge and the consequent pressure losses from the porous skin to the inlet of the compressor. This component is related to pressure and airfoil shape and in [10] is considered as a pressure drag component. However, it is considered an internal drag taking into account that the suction pump needs to restore the total head of the sucked air to that of the free-stream by discharging it at free-stream velocity. Hence it is approximated to be scaled with the free-stream dynamic pressure. The approximation is conservative for a "2D" approach. So the friction, pressure and suction drag coefficients are defined as:

$$C_{d_f} = C_{d_{f_{2d}}} \qquad C_{d_p} = C_{d_{P_{2d}}} cos^3(\varphi_{ref}) \qquad C_{d_s} = C_{d_{s_{2d}}} \tag{21}$$

Finally:

$$C_{d_{prof}} = C_{d_f} + C_{d_p} \tag{22}$$

Once the drag parameters are found, in the case of the aerodynamic solver convergence issues, if the number of non-converged sections is not higher than 2 (for a wing division in 8 sections), the parameters are determined through a proper interpolation strategy. If too many sections are not converged, the tool will result in "$not - a - number$" as final parameter. In particular, depending on the parallelization strategy adopted (see Sec.IV), if sections are analyzed in series, the loop can be directly stopped after the maximum limit of not converged sections is overcome to save computational time during the optimization.

3. Step 3

The last stage determines the final aerodynamic and performance quantities. In particular, lift coefficient C_L is obtained in step 1 (Sec.III.A.1) and hence no other calculation is needed. The total wing profile drag $C_{D\,prof}$ (including wave drag as clarified at the beginning of Sec.III) is obtained by integrating the sectional profile drag $C_{d\,prof}$ along the span. The same strategy is used to compute the total suction drag coefficient C_{DSw}, in fact, it is obtained by the integration of the sectional suction drag coefficient C_{ds} along the span:

$$C_{D\,prof} = \frac{2}{S} \int_0^{b/2} C_{d\,prof}\,c\,dy \tag{23}$$

$$C_{Dw} = C_{D\,prof} + C_{Di} \tag{24}$$

$$C_{Dsw} = \frac{2}{S} \int_0^{b/2} C_{d_s}\,c\,dy \tag{25}$$

The total wing drag (Eq.24) is given by the sum of the wing profile drag and the induced one evaluated with AVL in step 1 (Sec.III.A.1). The term C_{DSw} takes into account pressure losses happening from the suction orifices to the compressor inlet, considering the approximations and methodology explained in Sec.III.A.2. From Eq.25, the power necessary for the suction system is derived, details are shown in IV.A.

B. Aerodynamic solver: MSES COCO-LILO

The aerodynamic solver responsible for drag evaluation considering BLS is given by the coupling of MSES and COCO-LILO. MSES is a two-dimensional, steady, compressible Euler solver developed by Drela at MIT [29]. The Euler equations and the integral boundary layer formulation are solved by applying a global Newton solution scheme. Viscous drag and wave drag are computed by integrating the momentum defects in the viscous and the inviscid (shock) wakes of the flow field, respectively. BLS cannot be applied in the official version of MSES, and hence other tools are needed for its application. In particular, the coupling of a COnical, COmpressible boundary layer solver (COCO) and a linear stability solver (LILO). The coupling needs as input a prediction of the pressure distribution. COCO represents a boundary layer solver developed by Schrauf et al. [27]. In particular, the tool incorporates the boundary layer suction effect. The airfoil pressure distribution from MSES and the suction distribution are given as inputs to COCO. The boundary layer equation system is numerically solved using the Newton method with a second-order backward finite difference scheme. The solution yields the velocity and temperature profiles of the boundary layer and their first and second derivatives with respect to the wall-normal coordinate system. These are inputs for the linear stability analysis performed by LILO. High accuracy is demanded to COCO outputs because they may substantially

**Table 1   critical N-factors [11].**

$\varphi_{le}[deg]$	NLF		HLFC	
	N_{CF}	N_{TS}	N_{CF}	N_{TS}
0	-	11.5	-	9.5
22.5	7	9	6.5	7

influence the linear stability analysis. Predictions from COCO are validated against results from other boundary-layer codes [38]. The boundary layer solver computes the laminar skin friction drag. LILO predicts the amplification rates of the disturbance frequencies by means of the linear local stability theory thanks to the solution of the eigenvalue problem of the Orr-Sommerfeld equation [28]. The tool cannot model the flow effects due to geometry variations and boundary layer thickness. The developing boundary layer is responsive to external disturbances, which trigger the growth of TSI and CFI [39]. These waves superimpose the laminar base flow and become unstable at the indifference Reynolds number. The amplification of these disturbance waves may be modelled by Linear Stability Theory (LST). The logarithmic amplification factor called N-factor at a streamwise coordinate location x [40] is defined as:

$$N = ln\left(\frac{a}{a_0}\right) = \int_{x_0}^{x} -\alpha_i dx \tag{26}$$

where x_0 is the position where the disturbance with frequency f and amplitude a_0 first becomes unstable. The factor $-\alpha_i$ is the amplification rate, while the quantity e^n gives the amplification ratio. The methodology works rather well in a low-disturbance environment. In the present research, a two N-factor method [41] is used to predict transition due to TSI and CFI. In fact, the methodology is able to take into account the combined effect of the two forms of instabilities. In particular, in Fig.4a, the critical curve correlating the two forms of instabilities at a given chord position is found using an incompressible approach for linear stability analysis. The transition occurs if the computed N-factor envelope curve, representing the curve tangent to all the N-factor curves at different frequencies, intersects the critical curve (Fig.4b). Outside the critical curve, the flow is assumed turbulent. Two different critical curves are drawn in Fig.4a: one represents the N-crit curve for NLF (dashed line), while the other shows the critical curve for HLFC application. The difference is given to the additional disturbances due to the porous skin. The two critical curves are obtained from experimental campaigns described in [42]: ATTAS, Fokker100, A320 HLFC VTP.

The chosen critical N-factors (N-crit) for the analysis are presented in Tab.1. The knee point of the critical curve is chosen as a conservative estimation of the N-crit (Fig. 4a). N-crit of 7 and 9 are chosen for NLF airfoils, while 6.5 and 7 for HLFC application, for CFI and TSI respectively in a swept wing case. In fact, for the unswept case, no cross-flow instability is considered. Due to the lack of experimentally validated N-factors curve in a compressible flow, incompressible LST is used in this study. The complete workflow of the aerodynamic solver, from MSES to COCO-LILO and its drag output, is presented in Fig.5. In particular, free-stream properties are used as input and then
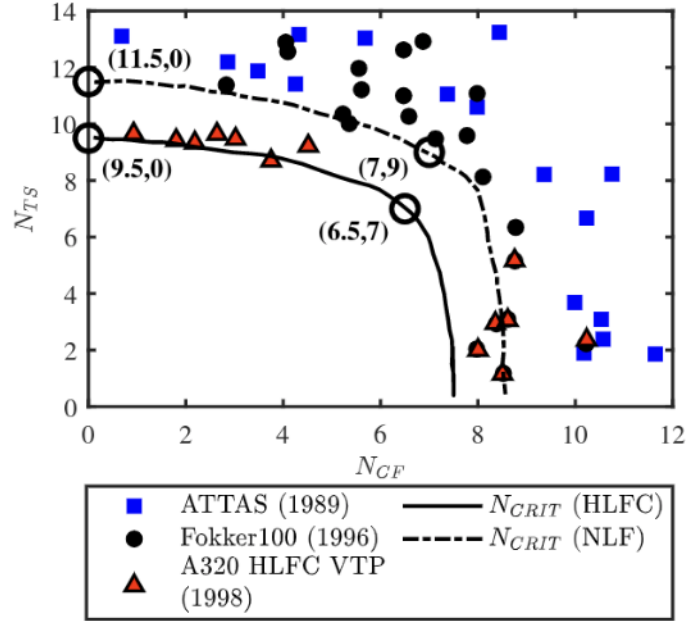
(a) N-factors correlation using incompressible LST based on flight test data, adapted from [43] and reported in [11]
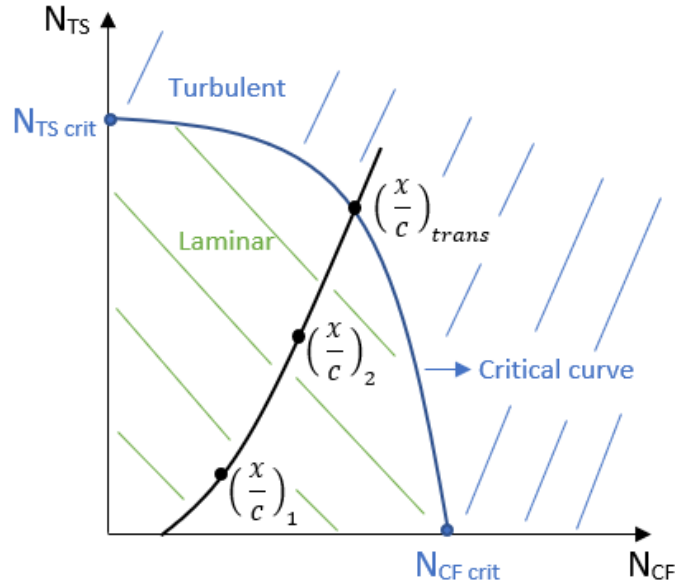
(b) Transition prediction through the two N-factor method, adapted from [30]

Fig. 4   N-factor transition prediction.

converted for 2D sections using Lock equivalence law [35] and a conical transformation as seen in Sec.III. At first, MSES runs assuming leading-edge transition (full turbulent flow) and $(x/c)_{ref} = 0.5$, the reference chord position is then updated considering the estimation of the shock wave position that next is fed back and used for the transformation between free-stream (3D) and sectional (2D) properties. The pressure distribution obtained by MSES is converted

in free-stream and given to COCO for boundary layer analysis. Data of temperature and velocity profiles, along with their derivatives, become input for the linear stability tool LILO which sets the transition point $(x/c)_{trans}$ as explained before. Skin friction evaluation comes from the boundary layer solver and represents the necessary laminar friction drag evaluation component. The loop is iterated until the transition position converges.
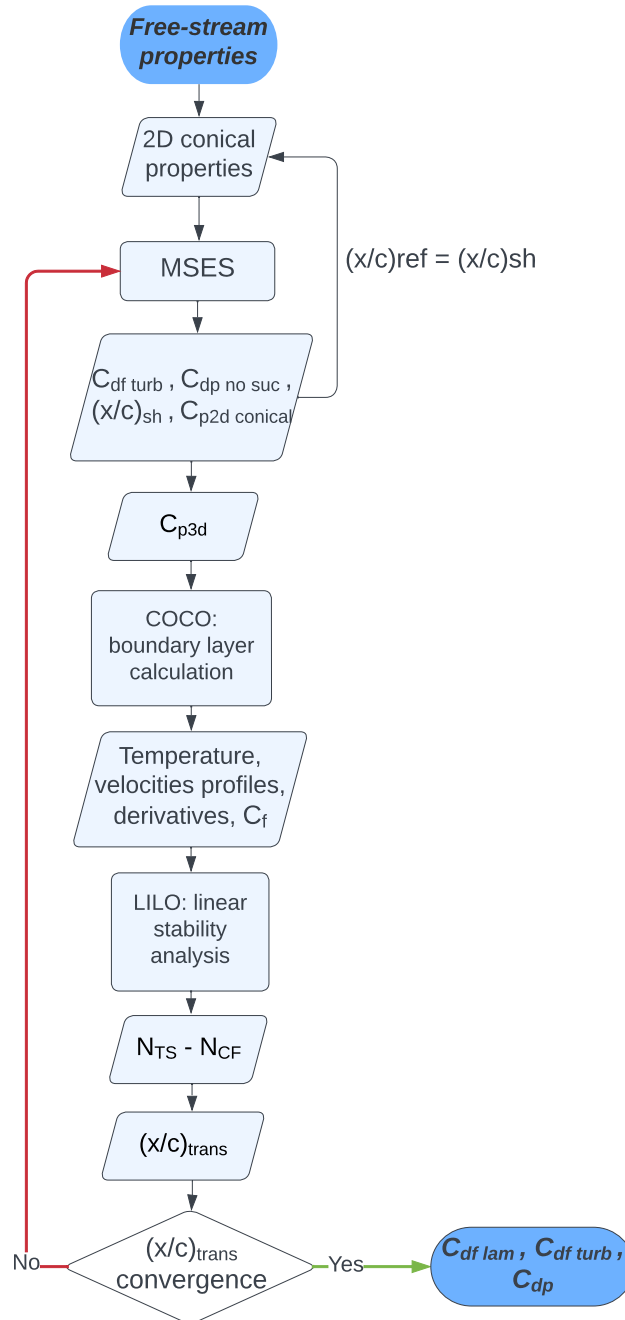
Fig. 5   MSES-COCO-LILO workflow.

Besides, the coupling COCO-LILO receives as input the effective sweep angle φ_{eff} and the attachment-line-

momentum-thickness Reynolds number $Re_{\theta,AL}$, used for the attachment-line transition criterion formulated by Pfenniger [44, 45]. In particular, considering a segment (as defined in Sec.III.A.2), $\varphi_{eff} = \varphi_{le} + \Delta\varphi_{eff}$, where $\Delta\varphi_{eff}$ is defined by Streit et al. [46] as:

$$\Delta\varphi_{eff} = \frac{t_{start} - t_{end}}{2s_{seg}} \tag{27}$$

in which, t_{start} and t_{end} represent the absolute thickness of the limiting sections of the selected segment. In the example shown in Fig.2, the sections in the first segment present as "start" thickness, the root thickness, while as "end" thickness, the thickness of the section at the kink. For the second segment, the two values are assigned to kink thickness and tip thickness, respectively. The parameter s_{seg} represents the spanwise dimension of the segment. The final output, consisting of drag, is decomposed into different components. The turbulent skin friction drag and the pressure drag are computed from MSES. MSES has no suction boundary condition and hence cannot model the effect of BLS (see the beginning of Sec.III.B). The laminar skin friction drag is computed from the higher fidelity boundary layer solver COCO. In fact, the boundary layer solver calculates only the laminar boundary layer and terminates at the flow separation point. The flow is assumed to transition at the separation point if the N_{crit} is not reached yet to avoid a laminar separation bubble. Boundary layer suction lowers the form drag due to the local thinning of the boundary layer [10], but considering that the developing boundary layer is thin near the leading edge under suction, the effect is assumed limited and then neglected. Finally, pressure drag coming from MSES is approximated as equal to the airfoil with no suction applied as a conservative estimation.

Total profile drag is:

$$C_{d_{profile}} = C_{d_{f_{laminar(COCO)}}} + C_{d_{f_{turb(MSES)}}} + C_{d_{p_{no-suction(MSES)}}} \tag{28}$$
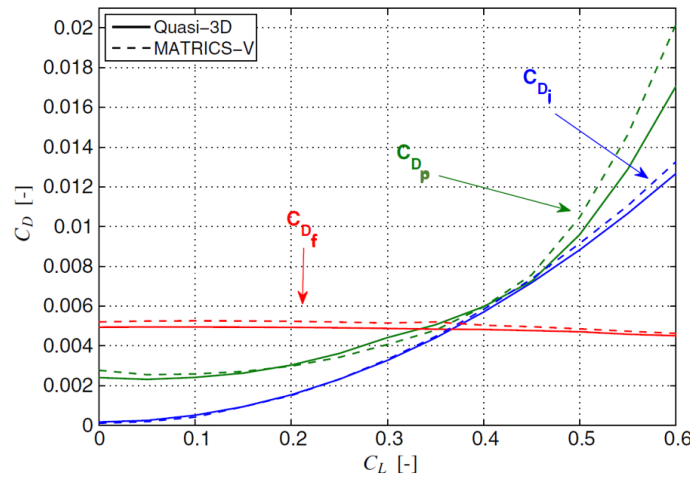
C. Validation

The validation process of tools that simulates the application of novel technologies may be challenging, especially due to the lack of databases like experimental tests or high fidelity analysis. The Q3D-HLFC validation can be divided into four steps.

The first step is represented by the validation of the Q3D strategy characterized by the analysis of 2D sections and their transformation to obtain 3d parameters of the wing. In particular, the standard Q3D characterized by a 2.5D analysis with a half-chord sweep line for transonic regime application is studied for turbulent application by Elham et al. [31] and shown in Fig.6. In Fig.6a, the drag coefficient is evaluated as a function of the Mach number, while in Fig.6b the C_D is evaluated with respect to the lift coefficient, wing-data of the Fokker 100 (full turbulent) are used. Besides, results obtained in Q3D are compared with the higher fidelity CFD tool output: MATRICS-V code [47]. The tool is based on fully conservative full potential outer flow in quasi-simultaneous interaction with an integral boundary layer

method on the wing. The code uses a far-field analysis method for drag prediction in transonic regime [48]. A good match is overall established, especially until $M = 0.8$ and $C_L = 0.5$. For higher values, in fact, instabilities start playing a more remarkable role and make this kind of approach less suitable. Besides, some differences may be generated by some limitations given by AVL in the lift distribution calculation and due to its Prandtl-Glauert compressibility model.
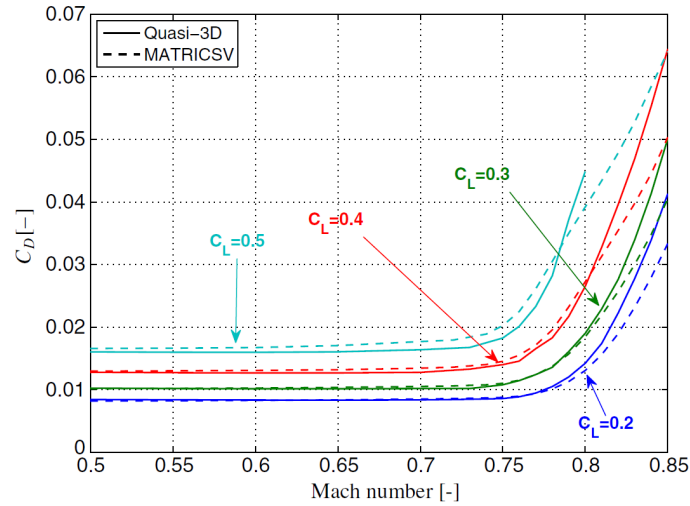
(a) Drag at different Mach and C_L, [31]

(b) Friction, pressure, and induced drag for the Fokker 100 wing in cruise condition, [31]

Fig. 6　Standard Q3D validation for transonic application, from [31].

Step 2) consists of validating the improvement and modification of the original Q3D given by the conical transformation and using the calculated shock-wave line as reference local sweep angle. The choice of using a conical transformation approach with variable shock-wave position, including attachment line and cross flow instabilities consideration (2.75D) is mainly given by the results presented by Streit et al. [32] and presented in Fig.7, for a backward-swept wing and natural laminar flow application. The 2.5D and 2.75D cases well approximate the pressure distribution from the 3D case. However, the raising of cross-flow instabilities is better captured by a conical transformation rather

than a 2.5D approach. In the cited article, note that this approach is suitable for an "infinite swept" wing, such that it does not capture the taper ratio effect of the wing. In the standard Q3D proposed by Elham et al. [31], this effect is essentially captured by 2D drag analysis for sections obtained normal to the sweep-line at a fixed percentage of the chord. Hence, the variation of the local sweep angle obtained from root to tip introduces the taper-ratio effect of the wing. The modified Q3D-HLFC presents the same correction but for a more accurate 2D analysis, considering a conical transformation of the airfoils and a calculated shock-wave line for the necessary reference sweep angles used in the transformation to 3d wing parameters. Besides, the instabilities presented in II are properly assessed with a 2.75D approach.
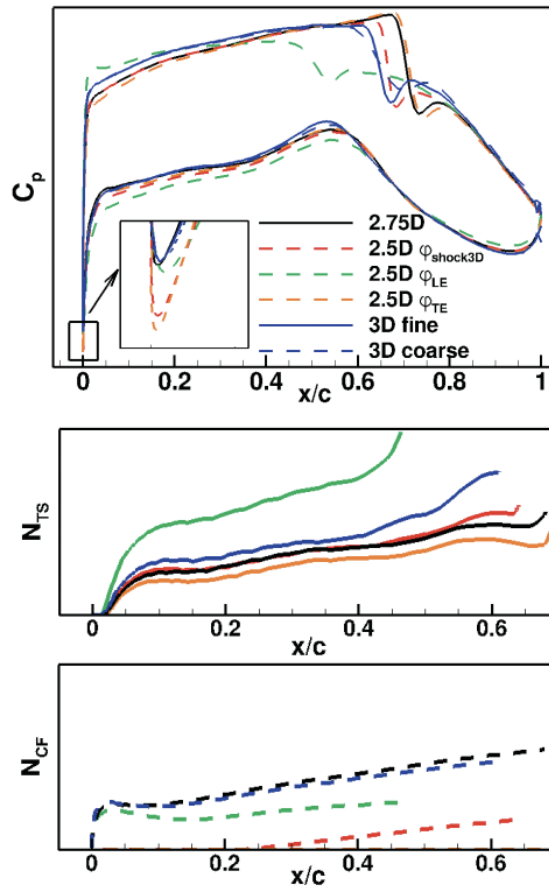
Fig. 7   Comparison between 2·5D, 2·75D and 3D upper side parameters for a wing section at the same lift for a NLF-BSW wing design by Streit et al. [32].

The third step presents a comparative analysis between the transition prediction and consequent drag evaluation of the coupled MSES COCO-LILO with respect to literature data. The use of linear stability theory is well-proofed and implemented in DLR research like in [38, 49], a test-case with validation including a conical transformation approach and the coupling of MSES and COCO-LILO is reported in [30]. In Fig.8, transition prediction, including CFI effect, is validated against experimental data from Dagenhart et al. [50]. In particular, an infinitely swept wing at 45 deg and

an angle of attack of 4 deg, using as airfoil section the NLF(2)0415 [11]. The analysis is performed considering the
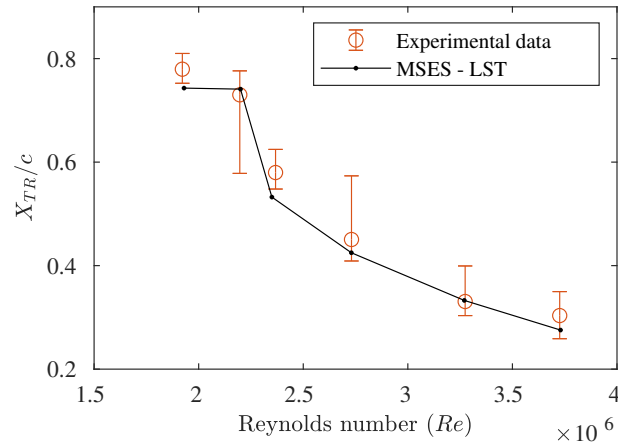

Fig. 8   MSES with LST validation for transition position with respect to Dagenhart et al. [50], taken from [11]

upper surface, experimental data are obtained using Naphthalene visualization for different Reynolds number. CFI become dominant for higher Reynolds number and predicted transition positions are within the uncertainty in the experiments. Figure 9 shows the lift coefficient with respect to the angle of attack and a drag polar analysis characterized by experimental data points compared with computational data [11]. Computations are obtained using MSES coupled with COCO-LILO and the default transition prediction method using Drela's envelope method available in MSES. The plots show a good agreement until 10 deg of the angle of attack, approximately at 1.6 as lift coefficient.
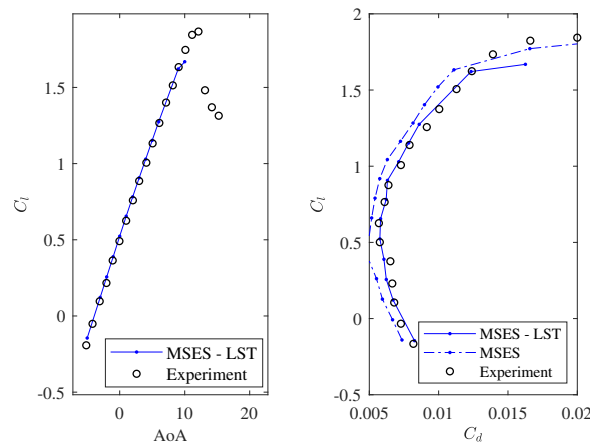
Fig. 9   MSES with LST validation of polar analysis with respect to Somers et al.[51]: NLF 0416 at M_∞= 0.4, $Re_c = 6 \cdot 10^6$, taken from [11].

The last point shows that the use of a 2.5D analysis, exploiting its less computational time, results in a good approach to initialize the optimization. A reference backward-swept wing is tested for a 2.5D and 2.75D analysis, and its pressure coefficient distribution is shown in Fig.10, for different sections, from root to tip. Wing drag presents a difference of 4.5

drag counts between the two analyses. The C_p has overall a good match. The exact sweep angle of the shock wave line (2.75D) is lower than the sweep angle obtained with the mid-chord sweep line (2.5D), causing a slight augmentation of the effective Mach number and hence drag but without severely affecting the pressure distribution. This shows that the use of a 2.5D methodology results in an acceptable optimization initializer.
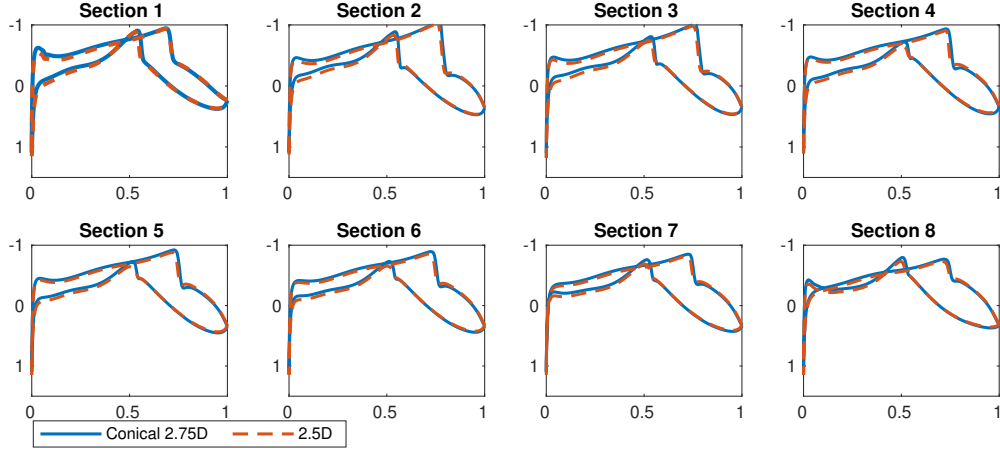

Fig. 10   Reference wing C_p distribution for 2.5D and 2.75D analysis.

IV. Wing aerostructural Multidisciplinary Design Optimization

The Multidisciplinary Design Optimization (MDO) framework consists of different modules: aerodynamic module, structural module, performance evaluation, and boundary layer suction system analysis. A global gradient-free optimization is performed using a genetic algorithm in Matlab. The use of a gradient-based optimization is discouraged, considering the difficulties in the proper computation of variable derivatives and possible convergence issues in the aerodynamic routine. The mutation scheme is the 'mutation adapt feasible', considered as suitable in case of bounds. It randomly generates directions that are adaptive with respect to the last successful or unsuccessful generation. The mutation chooses a direction and a step length that satisfies bounds and constraints. A default crossover fraction of 0.8 is used. The optimization problem can be written as follows:

$$
\begin{aligned}
&\text{Minimize} &&W_{fuel_s}(X) \\
&\text{w.r.t.} &&X = [cst_r \; cst_k \; cst_t \; b \; \varphi_{le} \; c_r \; \lambda \; c_k \; \epsilon_r \; \epsilon_k \; \epsilon_t] \\
&\text{subject to} &&\left(\frac{MTOW}{S_w}\right) \leq \left(\frac{MTOW}{S_w}\right)_{ref} \\
& &&X_{lower} \leq X \leq X_{upper}
\end{aligned}
\tag{29}
$$

The fitness function is characterized by fuel weight minimization. The first three groups of design variables represent an evolved version of the Class Shape Transform (CST) [52] method originally proposed by Kulfan [53]. They are used to define airfoil shape for the root, kink and tip sections. The modified version used Genetic Programming to fit better the shape of transonic airfoils that exhibit prominent rear loading [52], which is chosen for the current research. The wing geometry is defined by the span b, leading edge sweep angle φ_{le}, chord at root and kink, taper ratio λ, and the three sections twist angle ϵ. Each airfoil shape is defined through 14 design variables (7 for the upper surface and 7 for the lower one) and considering the other geometrical variables, a total of 50 design variables characterize the optimization problem. The optimization uses as reference a backward-swept wing designed in the SE^{2}A [20], adapted for the flight conditions found suitable for BLS application that is under investigation in this work. The airfoils are designed through an aerodynamic optimization similar to what was performed in [11] and substituted to the initial design in order to help the MDO with a proper starting point. The initial population is given by a data set of transonic and standard airfoils, while the geometrical parameters are built thanks to a Latin Hypercube sample matrix, using as boundaries a 25% of margin with respect to the reference. The problem can be split to ease the MDO computational time without affecting the probability of obtaining the optimum. In particular, an initial reduced optimization can be performed, scaling the reference airfoil shapes and reducing the 42 design variables used for root, kink and tip to just 3. In this case, a total of 11 variables are used. Besides, a 2.5D approach considering the reference sweep angle at 50% of the chord can be used, reducing the computational time needed to update the variables due to the calculation of shock-wave position inside the COCO-LILO loop for transition determination (see Sec.III.B). In fact, as seen in Sec.III, the computational time may be reduced, keeping an acceptable level of accuracy. Two different reduced optimizations are performed with a population of 60 individuals for 100 generations. The optimized results will be part of the initial population of 3 optimizations with all 50 design variables with the same number of individuals and generations. One last optimization is performed using a 2.75D conical approach with the update of φ_{ref} depending on the shock-wave location. The optimization is initialized with the results of previous optimizations while using the airfoils data set and Latin Hypercube sampling for the rest of the design variables and reducing the lower bound to 90%. In fact, all the results of the previous initial optimizations show that the optimizer points towards a slight augmentation of the span and leading edge sweep angle and little reduction of the chord root. Minimal variation of the twist is expected. The optimization proposed is a wing-optimization during cruise condition, but it is important to take into account also the other flight segments and conditions. The only constraint used is given by the wing loading smaller or equal to that of the reference aircraft to ensure performance at take-off and landing, taking into account the effect of wing loading on the stall speed:

$$\left(\frac{MTOW}{S_w}\right) \leq \left(\frac{MTOW}{S_w}\right)_{ref} \tag{30}$$

The constraint is implemented as a penalty on the fitness function, using a Heaviside function as shown in [12].

This strategy simplifies the analysis, avoiding the decrement of performance and potential errors that may arise during optimization when using a genetic algorithm in the presence of non-linear constraints. Some design considerations are checked at the end of the optimization. These are not defined as constraints; in fact, their presence would increment the computational effort, and this is not justified considering that preliminary results have suggested a low probability of their violation. They are:

$$AR \geq 8 \tag{31}$$

$$V_{f_{req}} \leq V_{f_{av}} \tag{32}$$

$$c_t \geq 1.3m \tag{33}$$

$$\frac{T}{W} \geq \left(\frac{T}{W}\right)_{ref} \tag{34}$$

The aspect ratio (AR) needs to be higher than a certain value (Eq.31) to guarantee climb performance. The condition is undoubtedly satisfied within the optimization thanks to the initial higher value. Besides, the fuel volume required has to be lower or equal to the available one, to be sure there is enough space to store fuel. Considering the tendency of the optimizer to increment the AR and the objective of fuel weight minimization, the design consideration should be satisfied. A chord tip smaller than 1.3 m is not feasible, but the condition is satisfied thanks to a lower bound of the taper ratio set at 0.255. The final condition is given by the thrust-to-weight ratio; a lower value could violate the constraint diagram defined for the reference aircraft at the preliminary-low-fidelity design phase. This is the most sensitive condition after the wing loading because, during the optimization, it is possible to achieve an increment of the maximum take-off weight (MTOW) even if a reduced fuel weight. In fact, this is highly dependent on the optimization strategy and design variables. In [22], a decrement of MTOW is reported for a reduced W_f but using a higher number of design variables, including the possibility of sizing the wing box panels through an aeroelastic approach. This is not possible in this framework, so an increment of MTOW is still possible. On the other hand, an increment in L/D and a reduction of drag suggest the possibility of being in a safe zone without violating the constraint. Besides, its implementation during the optimization is complex, considering the necessity of computing stall speed and parameters at take-off configuration, making the authors prefer a post-optimization check. More details are shown in Sec.V. The optimization framework can be graphically represented using the eXtended Design Structure Matrix (XDSM) [54] in Fig.11. The MDO starts with the aerodynamic tool Q3D used in inviscid mode (no profile drag calculation) to compute the distribution of the lift and the loads necessary for EMWET [55] to calculate the wing weight considering the maximum load factor $n_{max} = 2$ due to load alleviation. In this phase, no drag is necessary; hence, the tool is run in inviscid mode to save considerable computational time. Then, the Q3D-HLFC is run in full viscous mode for cruise condition ($n_{max} = 1$), obtaining lift and drag coefficients that become the input of the performance module to determine fuel weight. The boundary layer suction analysis routine receives suction drag and wing suction power parameters.
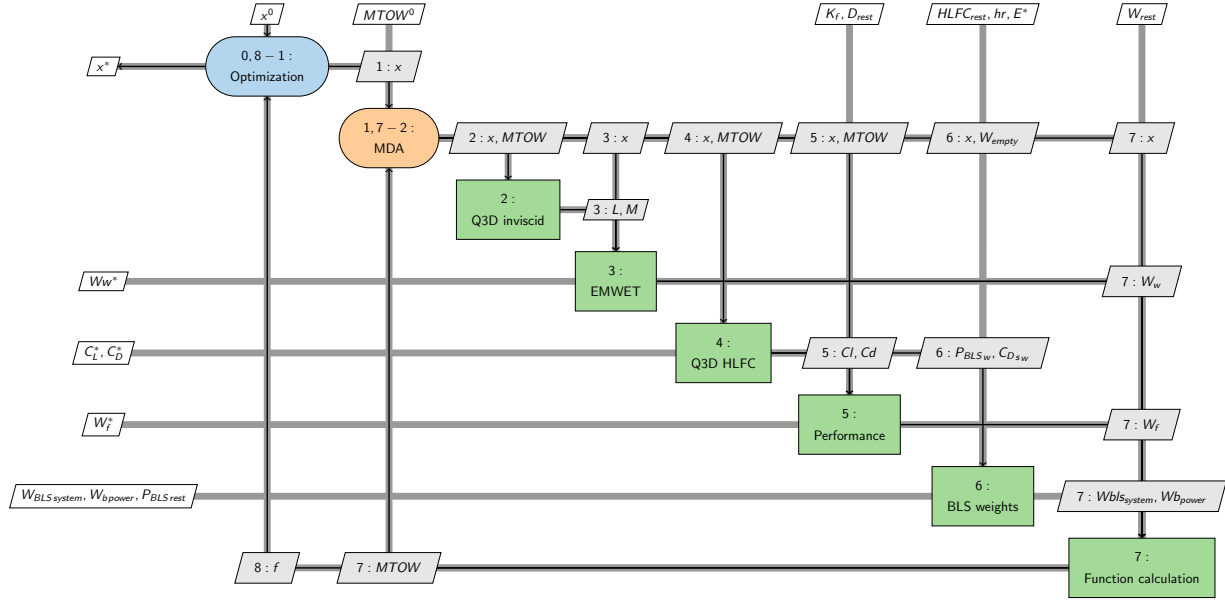
Fig. 11   XDSM for wing optimization.

It has as output all the suction power of the aircraft, and consequently, the battery is sized for the necessary power ($W_{battery-power}$) and the mass of suction system $W_{suc-system}$ is computed. All the weights are summed together with the fixed mass of the rest of the aircraft that is not changing during the wing optimization:

$$MTOW = W_w + W_f + W_{battery-power} + W_{suc-system} + W_{rest} \tag{35}$$

The iteration between the modules is stopped when a tolerance of $5e-4$ is satisfied for each weight component, except for the MTOW, which is set to have a maximum 50 kg variation as the difference with respect to the previous iteration. To summarize, an initial aerodynamic airfoil optimization is performed to obtain proper airfoils optimized for minimum drag and suction power. These are then used for a reduced aerostructural optimization, in which airfoils can be scaled without changing their shapes. The optimized vector initializes three full aerostructural optimizations (including airfoil CSTs as design variables), in which the Q3D-HLFC runs using the 2.5D approach. Finally, an aerostructural optimization in 2.75D mode is performed. The total computational time for such optimization is 240 hr using a 60-core Intel® Xeon(R) Gold 6252 CPU @ 2.10GHz. Generally, after 30 generations are analyzed, the optimization starts stalling, meaning not obtaining better solutions.

A. Aerodynamic module

The aerodynamic module consists of the use of Q3D-HLFC for lift and drag parameters. In particular, it may be launched in two different modes: inviscid and viscous. The first one is used when coupled with the structural

module (EMWET), and it is necessary to have just aerodynamic loads for maximum load factor without requiring drag calculation. The viscous mode is necessary for drag parameters, at cruise condition, and all the variables related to suction. In particular, Sudhi et al. [10] defined the equations representing the power of the suction system. A 2D suction distribution is given as input to the module, obtained from an airfoil shape optimization performed similarly to Sudhi et al. [11], to avoid the use of an excess number of design variables and speed up the MDO. Once the distribution is obtained, it can be scaled by a coefficient. An automatic procedure, as function of the lift coefficient, could be adopted for subsonic cases, scaling the suction with a factor $C_l^{-1/2}$ [56]. In this research, manual computations have shown that the procedure increases power absorption without any aerodynamic benefit, and hence the parameter has been tuned to 1.2. As an example, in Tab.2, the optimized wing configuration of this research is run, at C_L=0.36, for different scale coefficients, showing a minor variation of drag and keeping the power acceptably low. More details about the power are discussed in Sec.V.

Table 2   Suction scale parameter effect.

Suction scale parameter	Profile drag	Suction power [kW]
1.0	0.0040	82.15
1.2	0.00396	101.95
1.4	0.00407	117.57
1.6	0.00411	134.37

The suction system is represented schematically in Fig.12. The system is characterized by porous skin, plenum
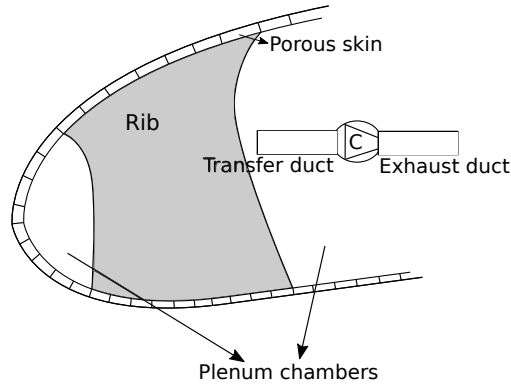

Fig. 12   Suction system scheme.

chambers and ducts connected to a compressor that will drive the system. The pump needs to restore the total head of the sucked air to that of the free stream by discharging it at a velocity equal to free-stream velocity. As an assumption, discharge velocity is considered equal to the free-stream velocity to eliminate sink drag:

$$P_{pump} = \frac{1}{\eta_{sp}} \int (p_0 - p_{0_{in}})v_0 \, ds \tag{36}$$

where η_{sp} is the efficiency of the suction pump, v_0 represents the local suction velocity, while p_0 and $p_{0_{in}}$ are the free-stream and inlet total pressure. A suction drag coefficient can be defined as:

$$C_{d_s} = \frac{\eta_{prop} P_{pump}}{\frac{1}{2}\rho U_\infty^3 c} \tag{37}$$

In particular, η_{prop} is the propulsive efficiency of the aircraft while c is the chord length. For simplicity, the two efficiencies are considered equal, $\eta_{sp} = \eta_{prop}$. Hence,

$$C_{d_s} = \int \frac{(p_0 - p_{0_{in}})}{\frac{1}{2}\rho U_\infty^2} \frac{v_0}{U_\infty} d\left(\frac{s}{c}\right) \tag{38}$$

$$C_{d_s} = \int \left(\frac{(p_0 - p_{0_e})}{\frac{1}{2}\rho U_\infty^2} + \frac{(p_e - p_{0_{in}})}{\frac{1}{2}\rho U_\infty^2}\right) \frac{v_0}{U_\infty} d\left(\frac{s}{c}\right) \tag{39}$$

where p_{0_e} is the total pressure at the edge of the boundary layer. In the ideal case of no pressure losses for example in the absence of porous skin and ducts, $p_{0_{in}} = p_{0_e}$. By applying the Bernoulli equation between free-stream and boundary layer: $p_0 = p_e + \frac{1}{2}\rho U_e^2$. Defining C_p as the pressure coefficient in the sucked region, v_0 as local suction velocity and U_∞ as the free-stream velocity, s/c represents the adimensional suction length. Finally:

$$C_{d_s} = \int \left((1 - C_p) + \frac{(p_e - p_{0_{in}})}{\frac{1}{2}\rho U_\infty^2}\right) \frac{v_0}{U_\infty} d\left(\frac{s}{c}\right) \tag{40}$$

Equation 40 takes into account the pressure loss of the components represented in Fig.12. Power characteristics are subjected to different uncertainties, which are challenging to be completely considered. A way could be to consider the experimental activities performed in the DLR for the A320 fin [57]. In particular, the surface and duct distribution pressure reported may represent a reasonable estimation of the difference in pressure achieved at the compressor inlet. Hence, the same pressure loss can be adopted during wing optimization. Alternatively, an acceptable estimation is to consider a 30% increment of the ideal suction drag, especially for components like fuselage and tail not subjected to optimization and so variation of parameters expressed in Eq.40. As seen in Sec.III.A, the wing suction drag coefficient is obtained by proper integration of the sectional coefficient along the span:

$$C_{Dsw} = \frac{2}{S} \int_0^{b/2} C_{d_s} c \, dy \tag{41}$$

The required total wing suction power is:

$$P_w = \frac{1}{2}\rho V^3 S C_{Dsw} k_{actual} \tag{42}$$

26

where $k_{actual} = 1.3$ is applied to consider the efficiencies of compressor and electric components. The compressor efficiency is selected as 80%. The electric efficiencies used in literature for similar applications are selected between 95% and 99% in [58, 59], while in [60], these are between 95% and 98%. Hence, for this research, a global value of 96% is chosen. The efficiencies represent conservative values considering nowadays the fast-technological advancement, especially of electric components, pushed by the automotive field.

B. Structural module

The aircraft wing weight is estimated using the EMWET tool [55]. EMWET is a tool for wing weight estimation, in which the wing is decomposed into two parts: primary and secondary structure. The primary structure group is further decomposed into the so-called optimum and non-optimum structure weight contributions. The former contributions include the spar webs and the upper and lower equivalent panels of the wing box, whose weight is determined analytically, evaluating the amount of material required to carry the critical loads. The latter contributions include weight penalty items such as joints, attachments, cutouts, etc. These, together with the secondary weight contributions, such as fixed leading and trailing edges, high lift devices, and movables, are determined using empirical methods. EMWET is developed for conventional-metal wings and is calibrated using conventional transport aircraft with metal structures, hence the final wing weight is 'corrected' with a coefficient that so reduces the total wing weight computed before. In particular, the effects of structure layout and novel materials are assumed to reduce the empty weight by 20%. EMWET computes the primary structure weight using the aerodynamic loads obtained by the Q3D-HLFC during Step 1 (Sec.III.A.1). AVL is used to determine the lift distribution and pitching moment distribution. In this way, the Q3D-HLFC can run without drag computation, exploiting the high speed of the VLM computation without launching the tool in drag mode twice inside the loop between the aerodynamic-structural module shown in Fig.11. The local pitching moment coefficient is calculated at the quarter chord line at each strip. It includes the moment due to the wing sweep and the moment due to the airfoils camber. As explained in the previous sections, aerodynamic loads are determined considering a maximum load factor of 2 (Q3D-HLFC has $n = 1$ for wing-optimization) because of the use of load alleviation. In fact, the technology is thought to design structures with lower n_{max} thanks to the reduction of bending moments. Hence, the research is characterized by a lower value from the limit load factor of 2.5 obtained using CS 25.337 [61]. The use of a lower maximum-load factor to take into account the effect of the technology in reducing weights during the optimization is justified considering that different studies have been done using these assumptions to model the load alleviation effect like in [62, 63]. Moreover, these values assume that load alleviation can counter gust and maneuver loads by at least 20%, while flight safety, in the event of failure for the load alleviation system, is considered by assuming safety factors similar to conventional aircraft [20]. Wing box components like skin, stringers and spars caps are modelled using just one upper and one lower equivalent panel. Front and rear spars webs are modelled using vertical panels (Fig.13). The upper and lower panels are sized to withstand the bending moments,
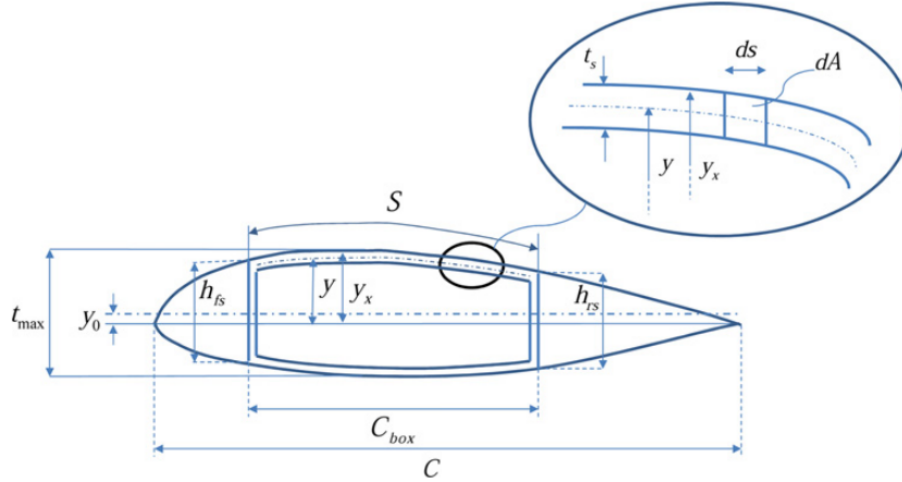
27

Fig. 13 Wing box [55].

whereas the spar webs are sized based on shear loads. Rib pitch is a parameter used to size the upper equivalent panels, but ribs weight contribution is estimated through an empirical method. The front and rear spars are located at 20% and 70% of the local chord.

The methodology was demonstrated to have an average error in the order of 2% [55]. More details about EMWET are presented in [55].

C. Suction system module

The routine is implemented to compute the extra mass necessary to carry on board because of the use of the boundary layer suction system, this includes the battery designed for supplying the BLS power computed in the aerodynamic module (see Sec.IV.A) and the weight of the suction system itself, made of compressors, electric components, wiring as an example.

1. Battery sizing

The battery, which provides energy for the suction, is sized considering the total actual power for wing suction plus the rest part of the aircraft, like the horizontal-vertical tail and the fuselage. The horizontal and vertical tail power is computed considering manually the C_{D_s} and then considering a 30% increment for pressure loss for porous skin and ducts and another 30% for compressor and electric component efficiencies. The suction drag coefficient of the fuselage is found thanks to data published in Beck et al. [9], analogous efficiencies are used for the fuselage. The battery weight is given by:

$$W_{b_{power}} = \frac{(P_w + P_{rest}) \cdot hr}{E^*} \tag{43}$$

28

where P_w is the actual wing power while P_{rest} is given by the sum of the actual powers from the horizontal-vertical tail and the fuselage. The parameter hr represents the number of hours for potential application of the BLS, it is calculated considering the design cruise Mach number 0.78 and the Top-Level Requirement (TLR) range of 4604 km. The specific energy density E^* is selected as 700 Wh/kg as described in [20] where the reference SE^{2}A aircraft is studied (the reader should be advised that in the present work, data are updated for higher speed case).

2. Suction system weight

The weight of the suction system is computed as the sum of the horizontal-vertical tail suction system plus the wing suction weight and then the fuselage contribution, also considering the weight increment for the skin thickness. Karpuk et al. [20] use a fraction of Operating Empty Weight (OEW) to define the total weight due for the vertical and horizontal tail suction system conservatively. In particular, the values are obtained from [64, 65]. Hence:

$$W_{BLS_{VT}} = 16\%OEW \tag{44}$$

$$W_{BLS_{HT}} = 11\%OEW \tag{45}$$

The wing suction system weight is computed proportionally starting from the value of the vertical tail.

$$W_{BLS_W} = \frac{S_{wetted_w} \cdot K_{suc_{c-w}} \cdot K_{suc_{s-w}} \cdot W_{BLS_{VT}}}{S_{wetted_{vt}} \cdot K_{suc_{c-vt}} \cdot K_{suc_{s-vt}}} \tag{46}$$

where S_{wetted} represents the wetted area, computed manually using CAD software for the vertical and horizontal tail (the optimization does not involve tail variation), while for the wing, the methodology described in Raymer [66] is used:

$$S_{wetted_w} = \frac{S_{exp_w}}{cos(\Gamma)} \cdot \left(1.977 + 0.52 \cdot \frac{1}{2}\left(\frac{t}{c}\Big|_{root} - \frac{t}{c}\Big|_{tip}\right)\right) \tag{47}$$

Γ represents the dihedral angle, while the thickness-to-chord ratio is referred to the free-stream sections at the root and tip. The parameter S_{exp_w} is the exposed wing area, given by the difference between the wing area and the portion related to the fuselage. This contribution could be approximated as the product between the chord root and the estimated segment of the fuselage, normal to the longitudinal axis, in which the wing attachment is located. The coefficients K_{suc_c} and K_{suc_s} represent the portion of suction interested in the surface chordwise and spanwise, respectively. They are referred for the wing (subscript "w") and vertical tail (subscript "vt"), they are 20% and 75% in this research.

The fuselage BLS system weight is characterized by two contributes, one given again by scaling the weight from the wing for the BLS system itself, and the other by the skin thickness that needs to be incremented for the fuselage with

respect to the other aircraft components. The first component is found applying a modified version from [20]:

$$W_{BLS_{fus}} = K_f \frac{S_{wetted_{fus}} \cdot K_{suc_{fus}}}{S_{wetted_w} \cdot K_{suc_{s-w}}} \cdot W_{BLS_W} \qquad (48)$$

in which the coefficient K_f represents the ratio of the actual suction drag coefficient of the fuselage and the mean actual wing suction drag coefficient applied to the suction area. Considering the definition of suction drag coefficient (C_{D_s}) explained in Sec.IV.A, the coefficient is already taking into account the limited chordwise application of suction. Hence the only parameters limiting the suction spanwise are applied: $K_{suc_{s-w}}$ for the wing and $K_{suc_{fus}}$ for the fuselage, considering the presence of small regions in which suction is not applied (as windows). This last parameter is set as 95% while the first, again, 75%. The wetted fuselage area is found by CAD tools, it represents the whole fuselage surface, in fact, the limitation related to the suction region is chordwise applied through the coefficient K_f and with the parameter $K_{suc_{fus}}$ as explained before. An additional mass estimation must be provided to estimate the potential mass penalty of the fuselage suction skin. The fuselage must have two shells: the porous shell, responsible for the boundary layer suction, and the structural shell, which carries loads and covers the cabin. The fuselage suction layer implies an increment of skin fuselage thickness and hence weight. In particular, from [20]:

$$W_{BLS_{skin-fus}} = 15\% \, t_{skin-fus} \, \rho_{mat} \, \pi \, D_{fus} \, L_{fus} \qquad (49)$$

where $t_{skin-fus}$ ([20]):

$$t_{skin-fus} = 3.2468 \cdot 10^{-8} \cdot W_{fus} + 7.5938 \cdot 10^{-4} \qquad (50)$$

The coefficient 15% in Eq.49 represents the skin-mass gain and represents the fraction of thickness of the porous shell with respect to the structural one, ρ_{mat} is the density of the metallic fuselage, while D_{fus} and L_{fus} are the diameter and length of the fuselage. Finally, the total weight increment for the BLS system in the fuselage:

$$W_{BLS_{fus-tot}} = W_{BLS_{fus}} + W_{BLS_{skin-fus}} \qquad (51)$$

D. Performance module

The module computes the fuel weight for the designed mission and an extra 5% for reserve. The methodology used is proposed by Roskam [67]. In particular:

$$W_f = 1.05(1 - M_{ff})MTOW \qquad (52)$$

M_{ff} is defined as the total fuel weight fraction. It represents the ratio between the total aircraft weight at the end of the flight mission and the total aircraft weight at its start. The fraction is determined from the Brequet equation for cruise mission and with the correction of a coefficient 0.9386 for the other segments of flight:

$$M_{ff} = 0.9386 \cdot e^{\left(\frac{-K_{ff}}{L/D}\right)} \tag{53}$$

The coefficient K_{ff} is related mainly to engine characteristics of fuel consumption. It can be empirically found reversing Eq.52 and Eq.53 using data from the reference aircraft. The aerodynamic efficiency L/D is calculated considering the output from the aerodynamic module and considering that the total drag is defined as $D = D_{wing} + D_{rest}$ with D_{rest} fixed from the reference configuration, in fact, the optimization is involving the wing only.

V. Results

The reference aircraft consists of a swept-back wing for mid-range application, designed in the SE^{2}A Cluster and presented in [20] but modified for high-speed research. Top-level requirements are shown in Tab.3. Optimizations described in Sec.IV result in the data presented in Tab.4.

Table 3   Reference BWD SE^{2}A aircraft.

Parameter	Value	Units
Cruise mach number	0.78	
Design cruise Altitude	10600	m
Maximum payload	19650	kg
Total range	4604	km
Ground take-off distance	1604	m

Table 4   Wing geometry data.

	b, m	φ_{LE}, deg	C_r, m	C_{kink}, m	taper ratio	ϵ_r, deg	ϵ_k, deg	ϵ_t, deg
Reference	43.4	16.0	6.4	4.3	0.26	2	1	-1
Optimized	45.0	19.0	6.0	4.4	0.26	1.96	1.25	-0.10

In particular, the optimized configuration results in an increased span to reduce induced drag and an increment of leading-edge sweep angle to lower the wave drag component (Fig.14). Hence, the wing presents an increment of aspect-ratio AR for a better aerodynamic efficiency that reduces drag and fuel burnt (see Eq.53). Besides, Fig.14 shows a low variation between the optimized wing and the same wing without the geometrical kink. In fact, the "yehudi" represents essentially a necessity to place the main landing gear without really giving aerodynamic benefits. Structural advantages are reached considering a higher root chord helping to sustain loads in an area with high stress. Twist angles present a limited variation from the reference values, they are not subjected to aeroelastic coupling. Compared to the
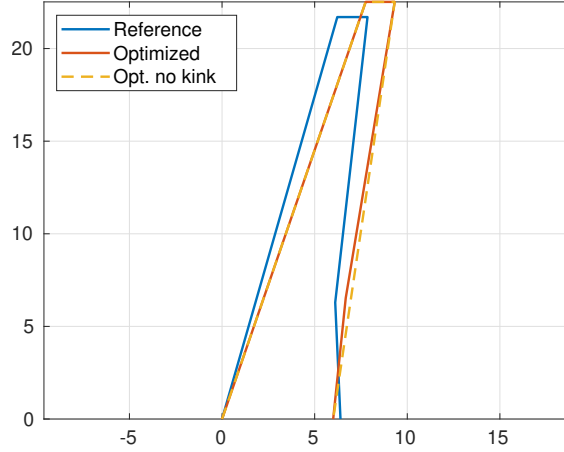
Fig. 14   Reference and optimized wing geometry.

reference one, details about the parameters and weights of the optimized wing are presented in Tab.5. In detail, Tab.5

Table 5   Optimization results.

	Reference	Optimized
AR	11.86	12.37
$C_{Lcruise}$	0.3603	0.3540
C_L/C_D	22.0	25.6
C_{Dwing}	0.00905	0.00673
ΔC_{Dwing}		-25.6%
$C_{Daircraft}$	0.01638	0.01383
$\Delta C_{Daircraft}$		-15.6%
$P_{suc_{wing}}$	84.7 kW	103.6 kW
$P_{suc_{rest}}$	149.3 kW	149.3 kW
W_w	5851 kg	6795 kg
$W_{b_{power}}$	1846 kg	1995 kg
$W_{BLS_{tot}}$	711 kg	736 kg
MTOW	64187 kg	64799 kg
W_f	8391 kg	7885 kg
ΔW_f		-6.0%

shows the reduction of the cruise lift coefficient ($C_{Lcruise}$) for the optimized configuration. In fact, the maximum take-off weight slightly increases, but this increment is well compensated by the increment in size and so the surface of the wing, leading to a reduction of the lift coefficient. Higher wing weight (W_w) is also expected due to the incremented dimension of the wing. The C_L/C_D is subjected to an improvement of about 16.4% thanks to the lower aircraft drag coefficient ($C_{Daircraft}$), reduced by 15.6% from reference. A sensitivity study showing the effect of different wing geometrical parameters on the weights and performance is shown in Fig.15. All the data are obtained from the optimized configuration and resizing it for different variables: span, leading edge sweep angle and maximum thickness-to-chord

ratio. In particular, each variable is modified, incrementing or decrementing its value and then resizing the aircraft to obtain the main weights and performance parameters. The purpose is to point out that the optimized wing reduces fuel weight thanks to all the trade-offs between disciplines. In Fig.15a, the increment of span causes higher wing weight due to the bigger wing size; this is translated into a higher maximum take-off weight. The reduced induced drag brings a reduction of the wing drag that does not compensate for the reduction of the lift coefficient, which leads to a lower aerodynamic efficiency L/D. Hence, the fuel weight increments. On the opposite, a reduction of the span allows a lower wing and maximum take-off weight but a higher wing drag due to higher induced drag for a lower aspect-ratio wing. The high increment in drag affects the L/D and hence brings more fuel weight. The increment of the leading-edge sweep angle in Fig.15b causes a stiffer wing and, therefore, an increment of its weight. A little variation of the MTOW is achieved. The wave drag reduction due to higher sweep does not compensate for the higher viscous drag related to the earlier transition to turbulent flow. As a consequence, the wing drag is incremented. The significantly higher $C_{D\,wing}$ reduces L/D and, as a result, the fuel weight raises. A lower φ_{le} reduces the wing and maximum take-off weight. Besides, the condition turns into higher wave drag due to a higher effective Mach number, resulting in higher wing drag. In fact, the optimum condition (at 0% of sweep angle variation) represents a trade-off between the two situations described. A low sweep angle raises substantially wave drag. At the same time, high φ_{le} makes viscous drag predominant due to instabilities (mainly cross-flow) triggering earlier transition and hence a condition with a lower portion of laminar flow. The last parameter analyzed is given by the maximum thickness-to-chord ratio Fig.15c. Its increment lowers the laminar flow region and strengthens the shock wave, causing higher wing drag. Thicker airfoils lower the wing weight and a minor variation of the MTOW. The reduction of L/D augments the fuel weight. Thinner sections lower W_w with a slight variation of the MTOW. Wing drag is augmented due to high viscous drag caused by a limited portion of laminar flow, while wave drag benefits from weak shock waves of thin airfoils. The lower L/D increments W_f.

The total weight of the BLS system plus the battery providing the required power for suction represents about 4% of the MTOW. The suction power of the wing is in line with the results found in literature, in fact, in Risse [30], a long-range aircraft presents around 200 kW of suction power for the wing and tail upper surface, converted for similar flight conditions to the present work. The configuration without tail and for M=0.78 is characterized by a wing suction power of $P_w \approx 154kW$, considering that the wing reference area is about 3.5 times the wing area for this research. In [68], a mid-range aircraft presenting a 52 m span and a wing area about 1.5 times the current wing, with $P_w \approx 86kW$ for probably just the upper surface, this is not clarified, but the project should involve laminarization through suction of the upper lifting surface. Hence, for all the above stated, the results match. Another way to lower wave drag component is airfoil-shape optimization characterized by weaker shock waves. The optimized airfoils are presented in Fig.16, showing the new configuration at the root, kink and tip, respectively. Besides, it can be noticed that an undercut at the lower surface is present at the tip, where no suction is applied, favouring front loading. In this case, the airfoil achieves
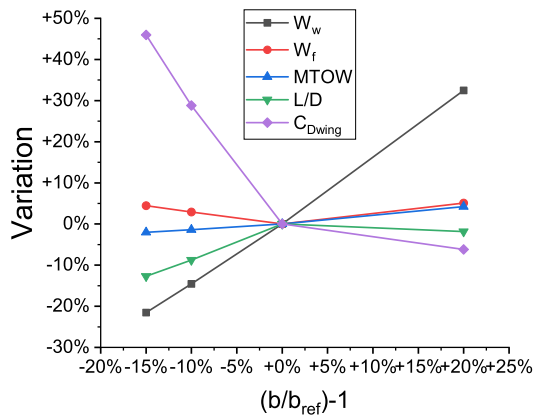
(a) Variation due to span
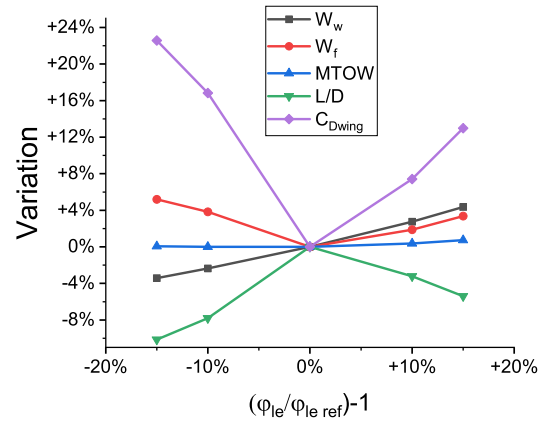
(b) Variation due to leading-edge sweep angle
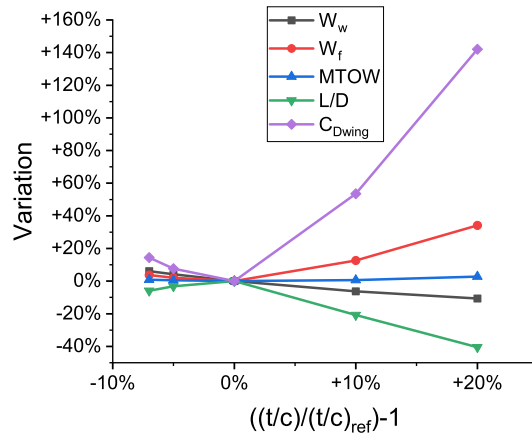
(c) Variation due to thickness-to-chord

Fig. 15   Weights and performance sensitivity study.

the desired lift while sustaining a weaker shock without imposing a more negative pitching moment that could bring infeasible trailing edge shapes [11, 69]. The new shapes allow better aerodynamic performance. It is observable that, generally, the optimized configuration presents a weakening of the shock waves helping the reduction of wing drag. The phenomenon is obtained especially for the lower surface. A comparison between the reference and the optimized configuration in terms of pressure distribution for different spanwise positions is shown in Fig.17. A complete overview of the interpolated contours of the pressure coefficients for each wing section with respect to the span is reported in Fig.18 and Fig.19.

The transition line is located approximately at 72% for the upper surface, while 52% for the bottom, for both configurations (Fig.20). At the tip, the bottom surface presents an early transition triggered by the reduced local Reynolds number. The reference wing shows an analogous laminar flow portion to the optimized configuration. In fact, the reference configuration is equipped with airfoils designed through a 2D sectional optimization to minimize drag, as
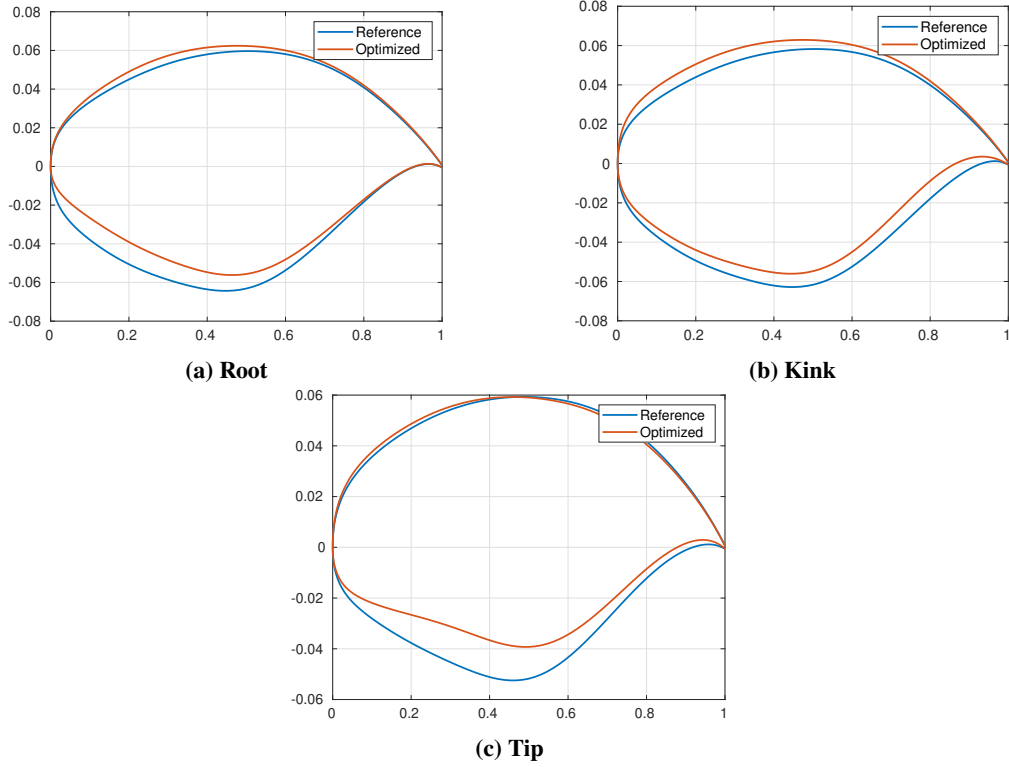
(a) Root

(b) Kink

(c) Tip

Fig. 16 Optimized airfoils.

Section η=0.143

Section η=0.429

Section η=0.571

Section η=0.714

Section η=0.857

Section η=1.000
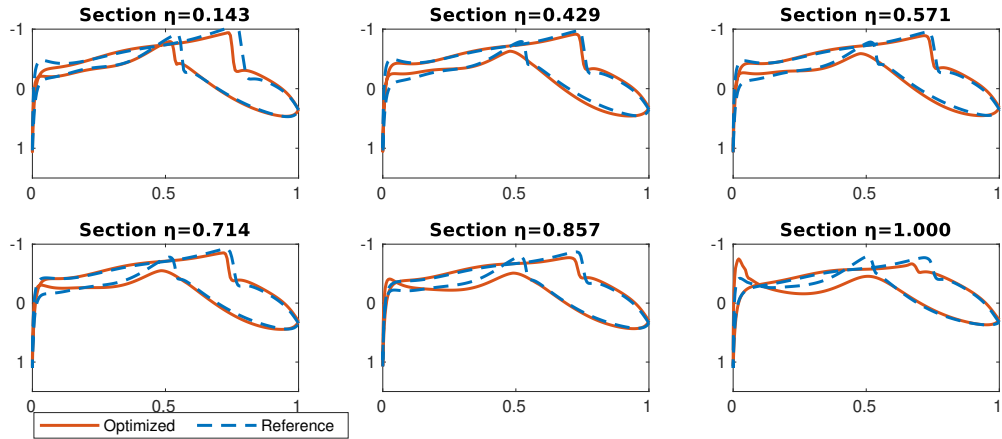
Optimized — — — Reference

Fig. 17 Pressure distribution comparison.

seen in Sec.IV. The effect of BLS is shown in Tab.6, in particular, the reference and optimized configuration are tested at the same flight conditions but with suction and without using the technology (NLF). The optimized configuration presents the highest relative wing drag reduction, lowering C_{D_w} for HLFC mode of about 28.7%.

The optimizer reduces the thickness of the airfoil (Fig.21) from root to tip, trying to find a configuration that maximizes laminar flow but without incrementing excessively wing weight. In fact, as seen in Fig.15c a too-low thickness raises wing weight that triggers maximum take-off weight translating into higher lift coefficient and, finally,
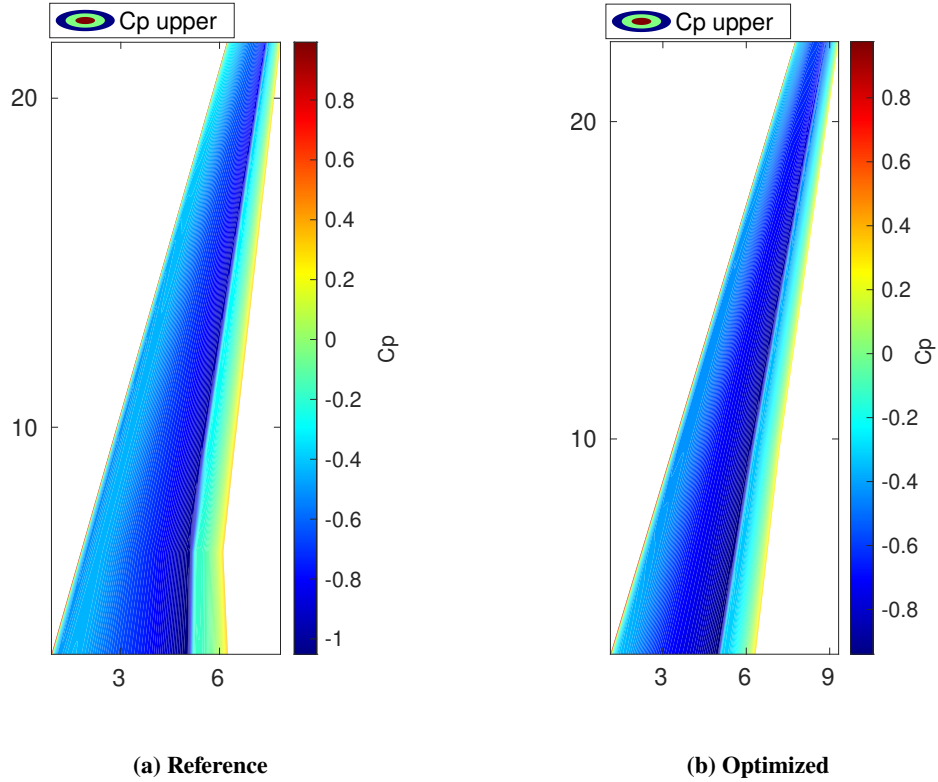
(a) Reference   (b) Optimized

Fig. 18   Interpolated surface pressure contours for the wing upper surface.

Table 6   Wing drag reduction due to BLS.

	Reference	Optimized
NLF	0.0101	0.0094
HLFC	0.0090	0.0067
ΔC_{Dw}	-10.4%	-28.7%

drag. Excessive thickness affects the laminar flow portion and implies a stronger shock wave, resulting in higher drag and lower aerodynamic efficiency.

As explained in Sec.IV, the optimized configuration needs to satisfy some design considerations. In particular, it is clear that a sufficient high AR is reached and a minimum of 1.3 m for the tip-chord. The wing loading constraint is satisfied during the optimization thanks to a penalty-method for the fitness function. Fuel volume is checked considering that the required fuel volume should be sufficiently high to store fuel and so less or equal to the available one. Defining the fuel weight W_f and fuel density ρ_f, in particular:
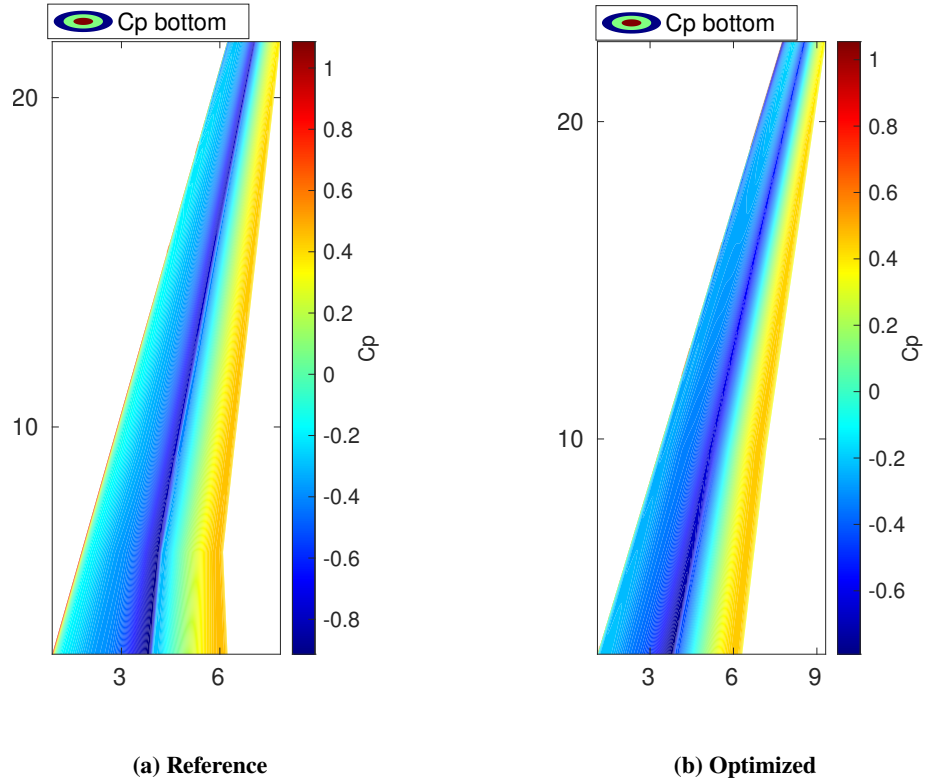
$$V_{f_{req}} = \frac{W_f}{\rho_f} \tag{54}$$

(a) Reference

(b) Optimized

Fig. 19   Interpolated surface pressure contours for the wing bottom.

(a) Reference wing
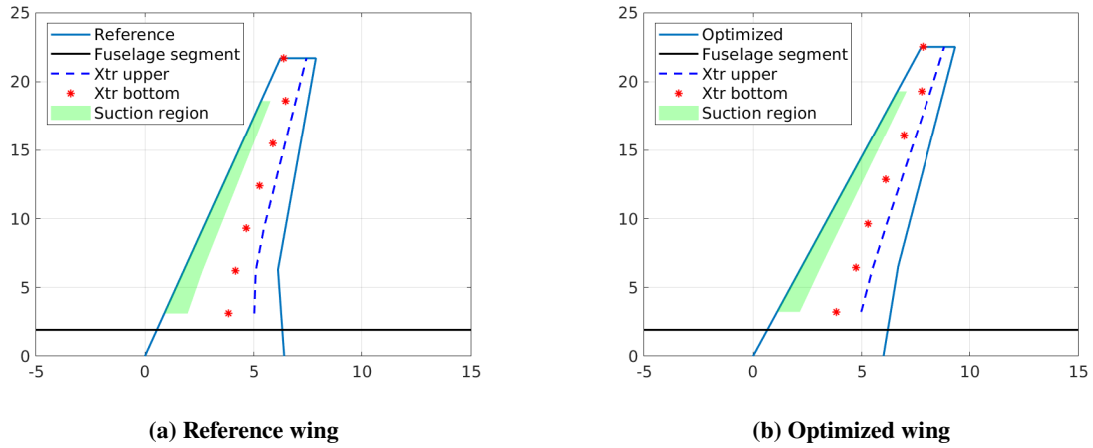
(b) Optimized wing

Fig. 20   Transition line position for reference and optimized configuration.

While the available fuel volume is defined in Scholz (Chapter 7) [70] and Torenbeek [71] as:

$$V_{f_{av}} = 0.54 \cdot (S_w^{1.5}) \cdot \frac{t}{c}\bigg|_{root} \cdot \frac{1}{\sqrt{AR}} \cdot \frac{(1 + \lambda\sqrt{\tau})}{(1 + \lambda)^2} \tag{55}$$

where S_w is the wing area, $\frac{t}{c}$ represents the thickness-to-chord ratio, while τ is the ratio between thickness-to-chord
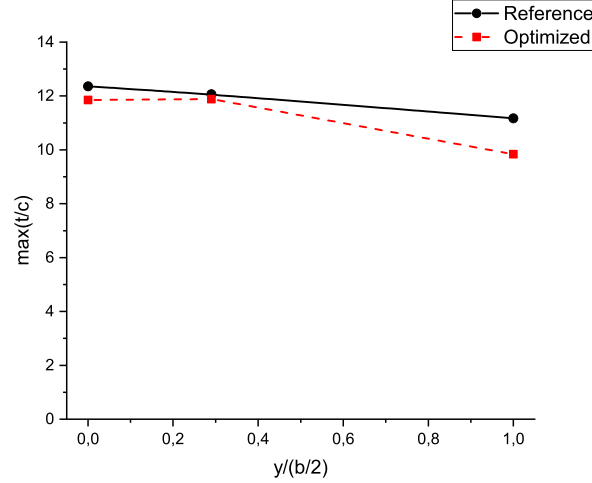
Fig. 21   Maximum thickness-to-chord ratio trend from root to tip.

ratio at the root and at the tip, λ defines the taper ratio. All the cited constraints are satisfied. The last condition is represented by the T/W at take-off, checking that the new performance capability will be enough to reach the reference take-off ground distance S_G defined in Tab.3. The take-off thrust-to-weight ratio is given by ([72]):

$$\frac{T}{W} = \frac{1.21}{9.81\rho C_{L_{max}} S_G} \cdot \frac{W}{S} + \left(\frac{0.605}{C_{L_{max}}}\right) \cdot (C_{D_{TO}} - \mu C_{L_{TO}}) + \mu \tag{56}$$

The maximum lift coefficient at take-off ("TO") is determined using DATCOM [73] methodology (also reported in [72]), in particular, MSES is used to find the airfoil $C_{l_{max}}$ at root, kink and tip and a correction is applied to consider 15 degrees of flap deflection at take-off for a single-slotted Fowler flap. A stall limit is projected, and then Q3D-HLFC at inviscid mode is launched at different angles of attack to understand when the stall limit is reached and, consequently, the maximum lift coefficient. The C_L at take-off is given again, launching Q3D-HLFC with no viscous drag, and then the value is corrected considering the ground effect. Drag components are given from Q3D-HLFC; the profile drag is then corrected for the flap deflection, while the induced one is corrected with the ground effect. The coefficient μ represents the ground friction constant and is taken equal to 0.04. Fig.22 shows the final values of wing loading and thrust-weight ratio, showing that the optimized configuration lies in the feasible design domain, given by the white area, with respect to the parameters evaluated in the preliminary phase for the reference aircraft.

VI. Conclusion

The present research shows the development of a quasi-three-dimensional aerodynamic solver for hybrid laminar flow control and natural laminar flow, including a shock-wave determination tool. A two-dimensional conical reference frame transformation of the sections and flow parameters is applied to evaluate drag at different wing positions. Drag is
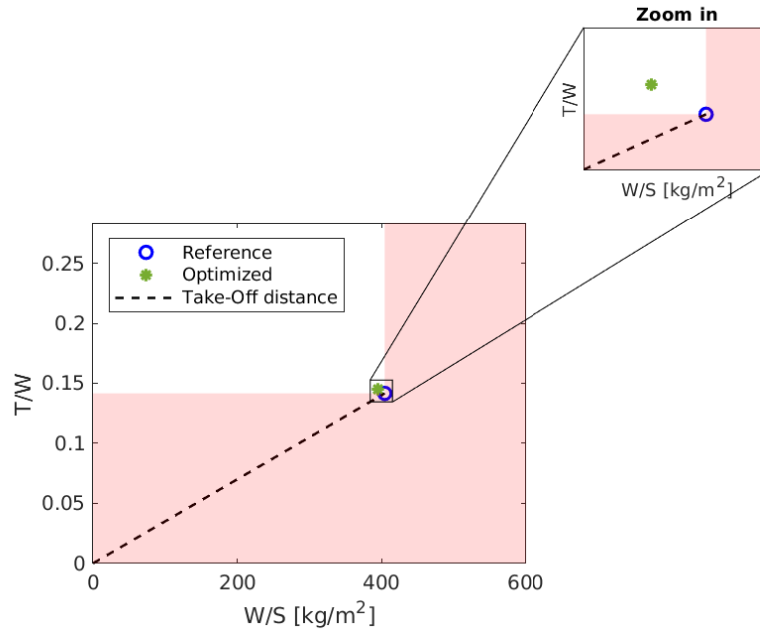
Fig. 22   Thrust to weight and wing loading consideration with respect to the reference configuration.

then converted to freestream (three-dimensional) direction. The tool is able to capture the effects of boundary-layer suction and hence provide accurate drag estimation with limited computational cost compared to higher fidelity software. The aerodynamic module is coupled with a structural analysis tool for wing weight calculation, considering the effects of load alleviation for lowering maximum loads and novel materials for lighter wings. The other modules present a boundary layer suction system analysis for battery and system weight estimation and a performance module that estimates the fuel weight to carry on board. The modules are part of a gradient-free optimization framework for fuel weight minimization. A backward-swept, mid-range aircraft designed in the Cluster of Excellence - SE^{2}A Sustainable and Energy Efficient Aviation is optimized. Final results show a limited increment of structural weights mainly due to the increment of wing span and leading edge sweep angle but with a reduction of fuel weight up to 6% thanks to improved aerodynamic properties. The boundary layer suction system implies extra weight due to the battery storing the energy needed and because of system components like compressors, wires, and electric motors. This increment is about 4% of the maximum take-off weight, well compensated by the aerodynamic advantages. In fact, the optimized configuration presents a reduction of 28.7% of wing drag with respect to the natural laminar flow case thanks to the suction application. Optimized airfoils present a thinner shape to lower wave drag, keeping laminar flow at 72% for the upper surface and 52% for the bottom. Proper trade-offs between disciplines are presented, showing the influence of design parameters on final weights and performance. Finally, some design considerations are checked for the optimized solution.

Funding Sources

References

[1] "Flightpath 2050-Europe's Vision for Aviation: Advisory Council for Aeronautics Research in Europe," , 2011.

[2] Braslow, A. L., "A history of suction-type laminar flow control with emphasis on flight research," *Monographs in Aerospace History Number 13, NASA*, 1999.

[3] Borodulin, V. I., Ivanov, A. V., Kachanov, Y. S., Mischenko, D. A., Örlü, R., Hanifi, A., and Hein, S., "Experimental and theoretical study of swept-wing boundary-layer instabilities. Three-dimensional Tollmien-Schlichting instability," *Physics of Fluids*, Vol. 31, No. 11, 2019, p. 114104. https://doi.org/10.1063/1.5125812.

[4] Joslin, R. D., and Streett, C. L., "The role of stationary cross-flow vortices in boundary-layer transition on swept wings," *Physics of Fluids*, Vol. 6, No. 10, 1994, pp. 3442–3453. https://doi.org/10.1063/1.868401.

[5] Swoboda, M., and Nitsche, W., "Shock boundary-layer interaction on transonic airfoils for laminar and turbulent flow," *Journal of Aircraft*, Vol. 33, No. 1, 1996, p. 100–108. https://doi.org/10.2514/3.46909.

[6] Giannelis, N. F., and Vio, G. A. and Levinski, O., "A review of recent developments in the understanding of transonic shock buffet," *Progress in Aerospace Sciences*, Vol. 92, No. 1, 2017, p. 39–84. https://doi.org/https://doi.org/10.1016/j.paerosci.2017.05.004.

[7] Krishnan, K. S. G., and Bertram, O., and Seibel, O., "Review of hybrid laminar flow control systems," *Progress in Aerospace Sciences*, Vol. 93, 2017, pp. 24–52. https://doi.org/10.1016/j.paerosci.2017.05.005.

[8] Spalart, P. R., and McLean, J. D., "Drag reduction: enticing turbulence, and then an industry," *Philosophical Transactions of the Royal Society A: Mathematical, Physical and Engineering Sciences*, Vol. 369, No. 1940, 2011, pp. 1556–1569. https://doi.org/10.1098/rsta.2010.0369.

[9] Beck, N., Landa, T., Seitz, A., Boermans, L., Liu, Y., and Radespiel, R., "Drag reduction by laminar flow control," *Energies*, Vol. 11, No. 252, 2018. https://doi.org/10.3390/en11010252.

[10] Sudhi, A., Elham, A., and Badrya, C., "Coupled boundary layer suction and airfoil shape optimization for HLFC application," *AIAA J.*, 2021. https://doi.org/10.2514/1.J060480.

[11] Sudhi, A., Radespiel, R., and Badrya, C., "Design Exploration of Transonic Airfoils for Natural and Hybrid Laminar Flow Control Applications," *Journal of Aircraft*, Vol. 60, No. 3, 2023, pp. 716–732. https://doi.org/10.2514/1.C036968.

[12] Mosca, V., Karpuk, S., Sudhi, A., Badrya, C., and Elham, A., "Multidisciplinary design optimisation of a fully electric regional aircraft wing with active flow control technology," *The Aeronautical Journal*, 2021, pp. 1–25. https://doi.org/10.1017/aer.2021. 101.

[13] Horst, P., Elham, A., and Radespiel, R., "Reduction of Aircraft Drag, Loads and Mass for Energy Transition in Aeronautics," *DLRK 2020*, September 2020. https://doi.org/10.25967/530164.

[14] Gröhlich, M., Böswald, M., and Winter, R., "An iterative eigenvalue solver for systems with frequency dependent material properties," *In Proceedings of the DAGA 2020*, 2020, pp. 900–903.

[15] Dähne, S., and Hühne, C., "Gradient Based Structural Optimization of a Stringer Stiffened Composite Wing Box with Variable Stringer Orientation," *Advances in Structural and Multidisciplinary Optimization*, 2018, pp. 814–826. https: //doi.org/10.1007/978-3-319-67988-4_62.

[16] Wunderlich, T. F., Dähne, S., Reimer, L., and Schuster, A., "Global Aero-Structural Design Optimization of More Flexible Wings for Commercial Aircraft," *Journal of Aircraft*, Vol. 58, No. 6, 2021, pp. 1254–1271. https://doi.org/10.2514/1.C036301.

[17] Hahn, D., Haupt, M., and Heimbs, S., "Passive Load Alleviation by Nonlinear Stiffness of Airfoil Structures," *AIAA SCITECH 2022 Forum*, 2022. https://doi.org/10.2514/6.2022-0318.

[18] Rossow, C.-C., von Geyr, H., and Hepperle, M., "The 1g-Wing, Visionary Concept or Naive Solution?" *DLR-IB-AS-BS-2016-121*, 2016.

[19] Liu, X., and Sun, Q., "Gust Load Alleviation with Robust Control for a Flexible Wing," *Shock and Vibration*, Vol. 2016, 2016. https://doi.org/10.1155/2016/1060574.

[20] Karpuk, S., Radespiel, R., and Elham, A., "Assessment of Future Airframe and Propulsion Technologies on Sustainability of Next-Generation Mid-Range Aircraft," *Aerospace*, Vol. 9, No. 5, 2022. https://doi.org/10.3390/aerospace9050279.

[21] Liem, R. P., Mader, C. A., Lee, E., and Martins, J. R. R. A., "Aerostructural design optimization of a 100-passenger regional jet with surrogate-based mission analysis," *2013 Aviation Technology, Integration, and Operations Conference*, 2013. https://doi.org/10.2514/6.2013-4372.

[22] Mosca, V., and Elham, A., "Investigations on the Potentials of Novel Technologies for Aircraft Fuel Burn Reduction through Aerostructural Optimisation," *Aerospace*, Vol. 9, No. 12, 2022. https://doi.org/10.3390/aerospace9120744.

[23] Kenway, G. K. W., Kennedy, G. J., and Martins, J. R. R. A., "Scalable parallel approach for High-Fidelity Steady-State aeroelastic analysis and adjoint derivative computations," *AIAA J*, Vol. 52, No. 5, 2014. https://doi.org/10.2514/1.J052255.

[24] Horst, P., Elham, A., and Radespiel, R., "Reduction of Aircraft Drag, Loads and Mass for Energy Transition in Aeronautics," *Deutsche Gesellschaft für Luft- und Raumfahrt - Lilienthal-Oberth e.V.*, 2021. https://doi.org/10.25967/530164.

[25] Schlichting, H., and Gersten, K., *Boundary-layer theory*, Springer, 2016.

[26] Poll, D., "Transition in the Infinite Swept Attachment Line Boundary Layer," *Aeronautical Quarterly*, Vol. 30, No. 4, 1979, pp. 607–629. https://doi.org/10.1017/S0001925900008763.

[27] Schrauf, G., "COCO-A program to compute velocity and temperature profiles for local and non local stability analysis of compressible, conical boundary layers with suction," *ZARM Technik report*, 1998.

[28] Schrauf, G., "LILO 2.1 User's guide and tutorial," *GSSC Technical Report*, Vol. 6, 2006.

[29] Drela, M., "Design and optimization method for multi-element airfoils," *Aerospace Design Conference*, 1993.

[30] Risse, K., "Preliminary Overall Aircraft Design with Hybrid Laminar Flow Control," *Phd thesis*, 2016.

[31] Mariens, J., Elham, A., and van Tooren, M. J. L., "Quasi-three-dimensional aerodynamic solver for multidisciplinary design optimization of lifting surfaces," *Journal of Aircraft*, Vol. 51, No. 2, 2014, pp. 547–558. https://doi.org/10.2514/1.C032261.

[32] Streit, T., Wedler, S., and Kruse, M., "DLR Natural and Hybrid Transonic Laminar Wing Design Incorporating New Methodologies," *The Aeronautical Journal*, Vol. 119, No. 1221, 2015, p. 1303–1326. https://doi.org/10.1017/S0001924000011283.

[33] Méheut, M., and Bailly, D., "Drag-Breakdown Methods from Wake Measurements," *AIAA Journal*, Vol. 46, No. 4, 2008, pp. 847–862. https://doi.org/10.2514/1.29051.

[34] Drela, M., and Youuungren, H., "Athena Vortex-Lattice Method," *Massachusetts Inst. of Technology, Cambridge, MA*, 2020. URL http://web.mit.edu/drela/Public/web/avl.

[35] Lock, R. C., "An Equivalence Law Relating Three- and Two-Dimensional Pressure Distributions," *Aeronautical Research Council Reports and Memoranda*, Vol. 3346, 1962.

[36] Kaups, K., and Cebeci, T., "Compressible Laminar Boundary Layers with Suction on Swept and Tapered Wings," *Journal of Aircraft*, Vol. 14, No. 7, 1977, p. 661–667. https://doi.org/10.2514/3.44614.

[37] Drela, M., *Flight Vehicle Aerodynamics*, MIT Press, 2014.

[38] Schrauf, G., Perraud, J., Vitiello, D., and Lam, F., "A comparison of linear stability theories using F1OO-flight tests," *15th Applied Aerodynamics Conference*, 1997. https://doi.org/10.2514/6.1997-2311.

[39] Saric, W. S., Reed, H. L., and Kerschen, E. J., "Boundary-layer receptivity to freestream disturbances," *Annual Review of Fluid Mechanics*, Vol. 34, No. 1, 2002, pp. 291–319. https://doi.org/10.1146/annurev.fluid.34.082701.161921.

[40] Van Ingen, J., "The eN method for transition prediction. Historical review of work at TU Delft," *38th Fluid Dynamics Conference and Exhibit*, 2008, p. 3830.

[41] Arnal, D., "Boundary Layer Transition: Predictions based on Linear Theory," *Special Course on Progress in Transition Modelling*, Vol. AGARD-R-793, NATO AGARD, 1994.

[42] Schrauf, G., "Large-Scale Laminar Flow Tests Evaluated with Linear Stability Theory," *Journal of Aircraft*, Vol. 41, No. 2, 2004, pp. 224–230. https://doi.org/10.2514/1.9280.

[43] Schrauf, G., and Von Geyr, H., "Simplified Hybrid Laminar Flow Control for the A320 Fin Part 2: Evaluation with the-Method," *AIAA Scitech 2021 Forum*, 2021. https://doi.org/10.2514/6.2021-1305.

[44] Pfenninger, W., "Some Results from the X-21A Program. Part I: Flow Phenomena at the Leading Edge of Swept Wings," *AGARDograph*, Vol. 97, No. 4, 1965, pp. 1–41.

[45] Pfenninger, W., "Laminar Flow Control—Laminarization," *Special Course on Concepts for Drag Reduction*, Vol. AGARD-R-654, NATO AGARD, 1977, p. 3.1–3.75.

[46] Streit, T., Wichmann, G., von Knoblauch zu Hatzbach, F., and Campbell, R. L., "Implications of Conical Flow for Laminar Wing Design and Analysis," *29th AIAA Applied Aerodynamics Conference*, 2011. https://doi.org/10.2514/6.2011-3808.

[47] van der Wees, A., van Muijden, J., and van der Vooren, J., "A Fast and Robust Viscous-Inviscid Interaction Solver for Transonic Flow About Wing/Body Configurations on the Basis of Full Potential Theory," *23rd Fluid Dynamics, Plasmadynamics, and Lasers Conference*, 1993, p. 1993–3026. https://doi.org/10.2514/6.1993-3026.

[48] van der Vooren, J., and van der Wees, A. J., "Inviscid drag prediction for transonic transport wings using a full-potential method," *Journal of Aircraft*, Vol. 28, No. 12, 1991, pp. 869–875. https://doi.org/10.2514/3.46111.

[49] Schrauf, G., and Horstmann, K. H., "Linear Stability Theory Applied to Natural and Hybrid Laminar Flow Experiments," *Aerodynamic Drag Reduction Technologies*, 2001, pp. 157–163.

[50] Dagenhart, J. R., and Saric, W. S., "Crossflow stability and transition experiments in swept-wing flow," *Tech. rep.*, 1999. URL https://www.cs.odu.edu/~mln/ltrs-pdfs/NASA-99-tp209344.pdf.

[51] Somers, D. M., "Design and Experimental Results for a Natural-Laminar-Flow Airfoil for General Aviation Applications," *NASA Technical report*, 1981.

[52] Powell, S., and Sóbester, A., "Application-specific class functions for the Kulfan transformation of airfoils," *13th AIAA/ISSMO Multidisciplinary Analysis and Optimization Conference 2010*, 2010. https://doi.org/10.2514/6.2010-9269.

[53] Kulfan, B. M., "A Universal Parametric Geometry Representation Method - "CST"," *45th AIAA Aerospace Sciences Meeting and Exhibit, American Institute of Aeronautics and Astronautics*, 2007. https://doi.org/10.2514/6.2007-62.

[54] Lambe, A. B., and Martins, J. R. R. A., "Extensions to the design structure matrix for the description of multidisciplinary design, analysis, and optimization processes," *Struct. Multidiscip. Des. Optim.*, Vol. 46,, 2012, p. 273–284. https://doi.org/10.1007/s00158-012-0763-y.

[55] Elham, A., La Rocca, G., and van Tooren, M. J. L., "Development and implementation of an advanced, design-sensitive method for wing weight estimation," *Aerospace Science and Technology*, Vol. 29, No. 1, 2013, pp. 100–113. https://doi.org/10.1016/j.ast.2013.01.012.

[56] van de Wal, H. J. B., "Design of a Wing with Boundary Layer Suction Redesigning the Wing of the Eaglet," *Master's thesis, Delft University of Technology*, 2010.

[57] Horn, M., Seitz, A., and Schneider, M., "NOVEL TAILORED SKIN SINGLE DUCT CONCEPT FOR HLFC FIN APPLICATION," *7TH EUROPEAN CONFERENCE FOR AERONAUTICS AND SPACE SCIENCES (EUCASS)*, 2017. https://doi.org/10.13009/EUCASS2017-44.

[58] Jansen, R. H., Bowman, C., Jankovsky, A., Dyson, R., and Felder, J. L., "Overview of NASA Electrified Aircraft Propulsion (EAP) Research for Large Subsonic Transports," *53rd AIAA/SAE/ASEE Joint Propulsion Conference 2017*, 2017, p. 2202. https://doi.org/10.2514/6.2017-4701.

[59] Aigner, B., Stumpf, E., Hinz, A., and De Doncker, R. W., "An Integrated Design Framework for Aircraft with Hybrid Electric Propulsion," *AIAA Scitech 2020 Forum*, 2020. https://doi.org/10.2514/6.2020-1501.

[60] Hepperle, M., "Electric Flight - Potential and Limitations, Energy Efficient Technologies and Concepts of Operation," *AVT-209 Workshop on Energy Efficient Technologies and Concepts Operation*, 2012. URL https://elib.dlr.de/78726/.

[61] "Certification Specifications and Acceptable Means of Compliance for Large Aeroplanes CS-25," 2020. URL https://perma.cc/9K76-KJPW.

[62] Hahn, D., and Haupt, M., "Exploration of the effect of wing component post-buckling on bending-twist coupling for nonlinear wing twist," *CEAS Aeronautical Journal*, 2022. https://doi.org/10.1007/s13272-022-00586-2.

[63] Handojo, V., Himisch, J., Bramsiepe, K., Krüger, W. R., and Tichy, L., "Potential Estimation of Load Alleviation and Future Technologies in Reducing Aircraft Structural Mass," *Aerospace*, Vol. 9, No. 8, 2022. https://doi.org/10.3390/aerospace9080412.

[64] Krishnan, K. S. G., and Bertram, O., "ASSESSMENT OF A CHAMBERLESS ACTIVE HLFC SYSTEM FOR THE VERTICAL TAIL PLANE OF A MID-RANGE TRANSPORT AIRCRAFT," *Deutscher Luft- und Raumfahrtkongress*, 2017.

[65] Srinivasan, G. K., and Bertram, O., "Preliminary Design and System Considerations for an Active Hybrid Laminar Flow Control System," *Aerospace*, Vol. 6, No. 10, 2019, p. 109. https://doi.org/10.3390/aerospace6100109, URL http://dx.doi.org/10.3390/aerospace6100109.

[66] Raymer, D., *Aircraft Design: A Conceptual Approach, 6th Edition*, AIAA Education Series, American Institute of Aeronautics and Astronautics, 2018. https://doi.org/10.2514/4.104909.

[67] Roskam, J., *Airplane design, Part, I: Preliminary sizing of airplanes*, DARcorporation, Lawrence Kansas, 1986.

[68] Effing, T., Schültke, F., and Stumpf, E., "HLFC-optimized retrofit aircraft design of a medium-range reference configuration within the AVACON project," *CEAS Aeronautical Journal*, Vol. 12, 2021. https://doi.org/10.1007/s13272-021-00510-0.

[69] Pfenninger, W., Viken, J., Vemuru, C. S., and Volpe, G., "All Laminar Supercritical LFC Airfoils with Natural Laminar Flow in the Region of the Main Wing Structure," *Turbulence Management and Relaminarisation*, edited by H. W. Liepmann and R. Narasimha, Springer Berlin Heidelberg, Berlin, Heidelberg, 1988, pp. 349–405.

[70] Scholz, D., *Aircraft Design -an Open Educational Resource (OER) for Hamburg Open Online University (HOOU)*, 2021. URL https://www.fzt.haw-hamburg.de/pers/Scholz/indexE.html.

[71] Torenbeek, E., *Synthesis of subsonic airplane design*, Delft University Press, 1978.

[72] Gudmundsson, S., *General Aviation Aircraft Design Applied Methods and Procedures, 2nd edition*, Butterworth-Heinemann, 2021.

[73] Hoak, D., *USAF Stability and Control DATCOM*, Flight Control Division, Air Force Flight Dynamics Laboratory, 1978.